공학석사 학위논문

Topology Optimization and Performance Evaluation on Vortex-type Passive Fluidic Diode for Advanced Nuclear Reactors

차세대 원자로의 **Vortex-type** 피동형 유동제어기의 위상최적화 및 성능평가

2018 년 2 월

서울대학교 대학원
에너지시스템공학부
임 도 균

Topology Optimization and Performance Evaluation on Vortex-type Passive Fluidic Diode for Advanced Nuclear Reactors

차세대 원자로의 Vortex-type 피동형 유동제어기의
위상최적화 및 성능평가

지도교수 김 응 수

이 논문을 공학석사 학위논문으로 제출함
2018년 2월

서울대학교 대학원
에너지시스템공학부
임 도 균

임도균의 석사 학위논문을 인준함
2018년 2월

위 원 장	조 형 규	(인)
부위원장	김 응 수	(인)
위 원	김 형 대	(인)

Abstract

Topology Optimization and Performance Evaluation on Vortex-type Passive Fluidic Diode for Advanced Nuclear Reactors

Do Kyun Lim
Department of Energy System Engineering
The Graduate School
Seoul National University

The fluidic diode (FD) is simple, passive device designed to provide small flow resistance in forward flow direction and large flow resistance in reverse flow direction. It plays a key role for importing passive core cooling system in advanced reactors such as hybrid loop-pool type Sodium Fast Reactors (SFRs) and Fluoride-salt-cooled High-temperature Reactors (FHRs). In nuclear industry, the vortex-type fluidic diode, one of fluidic diode consist of a circular chamber and two cylindrical port are preferred among fluidic diode because of its simplicity, easy maintenance feature. The performance of vortex-type fluidic

diode is expressed as diodicity (Di), and many studies have been conducted to enhance its diodicity after its first invention. In this study, the modified design for vortex-type fluidic diode is proposed using topology optimization technique to enhance the diodicity.

The topology optimization is one of optimization technique that finds out optimum material distribution in given domain. In this study, topology optimization is conducted for tangential port and chamber in 2-D domain and low-Reynolds laminar flow condition. Results with clear boundary and enhanced performance are selected as topology optimized design. Preliminary performance evaluation in 2-D geometry for this topology optimized design is conducted and 3-D part is designed based on 2-D geometry.

Experiment study is conducted to evaluate performance of 3-D topology optimized design. Pressure drop measurement and flow visualization experiment are conducted to topology optimized design and reference design. Stereolithography (SLA) 3-D printing technique is used to produce test sections and MIR-PIV technique is used to visualize flow inside the vortex-type fluidic diode. Velocity fields and pressure drop across vortex-type fluidic diode of each design are compared and it is found that reference design has better performance.

Flow characteristic study using 3-D CFD analysis is conducted to evaluate effect of design modification on pressure drop. CFD analysis is conducted by simulating experimental condition with laminar and turbulent flow model. Comparison between laminar flow model and turbulence model is made to select model which predicts experimental result more accurately. Variables obtained in CFD analysis such as flow field and total pressure are analyzed in detail. Based on this analysis result, contribution of each sub-part of vortex-type fluidic diode is

evaluated.

Keywords

Topology Optimization, Vortex-type Fluidic Diode, Computational Fluid Dynamics, Flow Visualization

Student Number: 2016-21306

List of Contents

Abstract ..... **i**

List of Contents ..... **iv**

List of Tables ..... **vi**

List of Figures ..... **vii**

Chapter 1. Introduction **1**

1.1 Background 1
1.2 Previous Studies 3
1.2.1 Vortex-type Fluidic Diode 3
1.2.2 Topology Optimization of Fluid Flow 3
1.3 Objectives 4

Chapter 2. Topology Optimization for Vortex-type Fluidic Diode **8**

2.1 Overview of Topology Optimization 8
2.2 Basic Equations and Algorithm 9
2.2.1 Fluid Dynamics Equations 9
2.2.2 Penalization 11
2.2.3 Constraints 11
2.2.4 Basic Algorithm 12
2.3 Vortex-type Fluidic Diode Design 12
2.3.1 Geometry and Design Domain 12
2.3.2 Optimization Process and Conditions 13
2.3.3 Optimization Results 14
2.3.4 Preliminary Performance Evaluation 15
2.3.5 Part Design 16

Chapter 3. Performance Evaluation using Experimental Study **29**

3.1 Experimental Setup 29
3.1.1 Test section 29
3.1.2 Test Loop 30
3.1.3 Flow Visualization System 31
3.1.4 Flow conditions 32

3.2 Experimental Results.....33
3.2.1 Pressure drop measurement.....33
3.2.2 Flow Visualization.....33

Chapter 4. Flow Characteristics Investigation using CFD Analysis.....45

4.1 Analysis Model and Conditions.....45
4.1.1 Geometry and Grid.....45
4.1.2 Models and Conditions.....46
4.2 Results.....48
4.2.1 Comparison with Experimental Results.....48
4.2.2 Evaluation of Effect of Sub-part on Pressure Drop.....49

Chapter 5. Summary and Conclusions.....63

5.1 Summary.....63
5.2 Recommendations.....64

Nomenclature.....66

References.....69

Appendix A. Safety Analysis for Advanced Nuclear Reactors.....72

국문 초록.....77

List of Tables

Table 2.1 Basic concepts of topology optimization for fluid flow (Serin Shin et al, 2017).....18
Table 2.2 Constraints of topology optimization (Serin Shin et al, 2017).....18
Table 2.3 Geometrical parameters for 2-D optimization geometry and design domain 19
Table 2.4 Information for gird used in optimization 19
Table 2.5 Optimization conditions and parameters.....20
Table 2.6 Information of gird for 2-D CFD analysis.....20
Table 2.7 2-D CFD analysis conditions.....21
Table 2.8 Geometrical parameters for 3-D topology optimized design 21

Table 3.1 Geometrical parameters for test sections.....36
Table 3.2 Image filter settings.....37
Table 3.3 Experimental flow conditions.....37

Table 4.1 Grid information 52
Table 4.2 Combination of turbulence model and inlet boundary condition 52
Table 4.3 Total pressure change in forward flow mode 53
Table 4.4 Total pressure change in reverse flow mode.....53

Table A.2 Detailed parameters for RELAP5 model (Zhang et al., 2008).....74
Table A.3 Initial condition for the transient analysis (Zhang et al., 2008) 74

List of Figures

Figure 1.1 Flow paths for primary coolant in hybrid loop-pool type SFRs (Zhang et al., 2008) 6
Figure 1.2 Flow paths for DRACS facility in FHRs (Holcomb et al., 2009) 6
Figure 1.3 Schematic drawing for vortex-type fluidic diode (Pandare and Ranade, 2015)..... 7
Figure 1.4 Flow configutaion of vortex-type fluidic diode (Lv, Q, et al., 2013).... 7

Figure 2.1 Brinkman penalization function 22
Figure 2.2 Basic algorithm of topology optimization for fluid flow.....22
Figure 2.3 2-D optimization geometry and boundary conditions 23
Figure 2.4 Divided design domains.....24
Figure 2.5 Grid for optimization geometry.....24
Figure 2.6 Optimization results : density function.....25
Figure 2.7 Optimization results : velocity field and streamlines 25
Figure 2.8 Geometry and grid for 2-D CFD analysis : T.O geometry.....26
Figure 2.9 Geometry and grid for 2-D CFD analysis : reference geometry.....26
Figure 2.10 2-D CFD analysis Results 27
Figure 2.11 Schematic drawing for tangential and axial port of 3-D T.O design ..28
Figure 2.12 Entire structure of 3-D T.O design 28

Figure 3.1 Geometry of reference design and T.O design.....38
Figure 3.2 3-D CAD model for test section.....39
Figure 3.3 Photo of test sections 39
Figure 3.4 Test loop.....40
Figure 3.5 Photo of flow visualization system.....40
Figure 3.6 Measurement plane for flow visualization.....41
Figure 3.7 Pressure drop measurement experiment results 41
Figure 3.8 PIV images and measurement region 42
Figure 3.9 The flow fields and measurement lines 42
Figure 3.10 Tangential velocity plots in measurement line 43
Figure 3.11 Comparison for normalized tangential velocity in measurement line 44

Figure 4.1 3-D CFD Analysis domain.....54

Figure 4.2 Grid for 3-D CFD analysis domain 55
Figure 4.3 Comparison of RANS model to RSM model (Pandare and Ranade, 2015).....55
Figure 4.4 Pressure drop comparison between experiments and CFD analysis : reference design 56
Figure 4.5 Pressure drop comparison between experiments and CFD analysis : T.O design.....57
Figure 4.6 Chamber tangential velocity field comparison between experiments and CFD analysis : Reference design.....58
Figure 4.7 Chamber tangential velocity field comparison between experiments and CFD analysis : T.O design.....59
Figure 4.8 Flow configuration inside the topology optimized design.....60
Figure 4.9 Schematic drawing for hypothetical lines and points.....60
Figure 4.10 Total pressure distribution along hypothetical line.....61
Figure 4.11 Normalized total pressure difference between hypothetical points....62

Figure A.1 RELAP5 model for hybrid loop-pool type SFRs (Zhang et al., 2008) 75
Figure A.2 Mass flow rate flow through PHX during LOFC transient (Zhang et al., 2008).....75
Figure A.3 Coolant Mass flow rates in first scenario (Lv, Q, et al. 2015).....76
Figure A.4 Coolant Mass flow rates in second scenario (Lv, Q, et al. 2015) 76

Chapter 1

Introduction

1.1 Background

The fluidic diode (FD) is a simple, passive flow control device designed to provide small flow resistance in forward flow direction and large flow resistance in reverse flow direction. In advanced nuclear reactors such as hybrid loop-pool type Sodium Cooled Fast Reactors (SFRs) and Fluoride-salt-cooled High-temperature Reactors (FHRs), the fluidic diode plays important role for importing passive core cooling system, by restricting flow according to operational conditions. The usage of fluidic diode in advanced reactors is explained in Fig 1.1 and 1.2.

The advanced nuclear reactors have system which removes decay heat from reactor core and the fluidic diode is connected to this system to control flow rate pass through it. In hybrid loop-pool type SFRs, the fluidic diode is connected to passive heat exchanger (PHX) as shown in Fig 1.1. In normal operation condition, reactor core is cooled by convective flow driven by primary pumps then heat transfers to intermediate heat exchanger (IHX). The bypass flow to decay heat removal system was restricted by the fluidic diode to minimize heat loss due to PHX. When pump is not operational, the decay heat generated from reactor core is

removed by buoyancy-driven natural circulation flow pass through PHX. Unlike normal operation condition, the fluidic diode provides low resistance for natural circulation flow to provide sufficient mass flow rate for remove decay heat (Zhang et al., 2008). In Direct Reactor Auxiliary Cooling System (DRACS) of FHRs, the fluidic diode is connected to DRACS heat exchanger as shown in Fig 1.2 and functions on the same manner as one in hybrid loop-pool type SFRs (Holcomb et al., 2009).

Vortex-type fluidic diode is one of existing concept of fluidic diode. It consists of a disc-shape chamber and cylindrical axial and tangential port as illustrated in Fig 1.3. Can be seen in Fig 1.4, it generates a high flow resistance by creating strong vortex across chamber in reverse flow mode, while generates relatively low resistance by creating radial flow distribution in forward flow mode. This concept has been widely used in nuclear systems due to its simplicity, easy maintenance feature. For this reason, it is one of promising candidate for fluidic diode in the advanced reactors mentioned above. In general, the performance of the vortex-type fluidic diode is defined as diodicity (Di), the ratio of pressure drop in reverse flow mode to forward flow mode under same boundary condition as below.

$$\mathrm{Di} = \frac{\Delta P_{reverse}}{\Delta P_{forward}} \tag{1.1}$$

It can be expected that the vortex-type fluidic diode with larger diodicity can enhance the passive safety feature. Thus, study to improve the performance of vortex-type fluidic diode can contribute to improve on passive safety feature of advanced reactors.

1.2 Previous Studies

1.2.1 Vortex-type Fluidic Diode

After the vortex-type fluidic diode concept was proposed, experimental and numerical studies have been continuously carried out to understand the design factors influencing its performance and the internal flow characteristics.

In early stage of research, design factors affecting vortex chamber, vortex-type fluidic diode applied only in reverse flow mode, were investigated by experimental study (Priestman, 1987). Recently, study for vortex-type fluidic diode was conducted in various perspective. A modified design for whole vortex-type fluidic diode was proposed and design factors affecting its performance were investigated using CFD analysis and experimental study (Kulkarni et al., 2008; Kulkarni et al., 2009). Other modified design only for tangential port was proposed for 50MW SFRs and its design parameters were studied to improve performance through full-scale experiment (Chikazawa et al., 2009).

Study to investigate flow inside the vortex-type fluidic diode was also conducted. A detailed CFD analysis for vortex type fluidic diode was conducted and various flow characteristics such as vortex transition and recirculation zone was analyzed (Pandare and Ranade, 2015).

1.2.2 Topology Optimization of Fluid Flow

Topology optimization is a one of mathematical technique for seeking out

optimum material distribution in design domain. Originally, it was well established within mechanical engineering of solids and structures, because new boundary can be acquired as a solution to optimization problem. Its application was extended to fluid flow area in order to minimize dissipated power in the fluid (Borrvall and Petersson, 2003). After its extension to fluid flow, it was used to design various devices related with fluid flow such as ventilation duct system (Othmer et al. 2007), 2-D fluidic diode (Lin et al., 2015) and the axial port of vortex-type fluidic diode (Shin et al., 2017).

In all of these researches, optimization was conducted in laminar flow regime, because topology optimization in turbulent flow regime is limited. Studies to adopt topology optimization technique to turbulence model is in progress (Yoon, 2016)

1.3 Objectives

The design of vortex-type fluidic diode has been continuously studied and modified since its first invention and further studies for its design and flow characteristics is still in progress. A new design different from the existing design can be proposed as a solution to topology optimization.

In this respect, the objectives of this study can be summarized as follows.

- Propose new modified design for vortex-type fluidic diode using topology optimization
- Evaluate performance of the modified design using experimental study (Pressure measurement, flow visualization)

- Investigate flow characteristics of vortex-type fluidic diode using detailed CFD analysis.

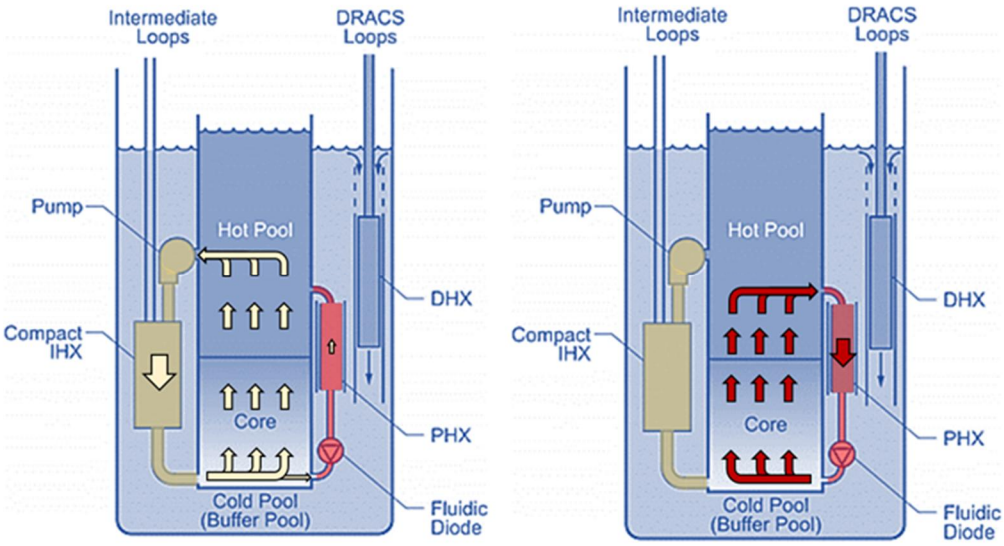

(a) Normal operation (b) LOFC transient

Figure 1.1 Flow paths for primary coolant in hybrid loop-pool type SFRs (Zhang et al., 2008)

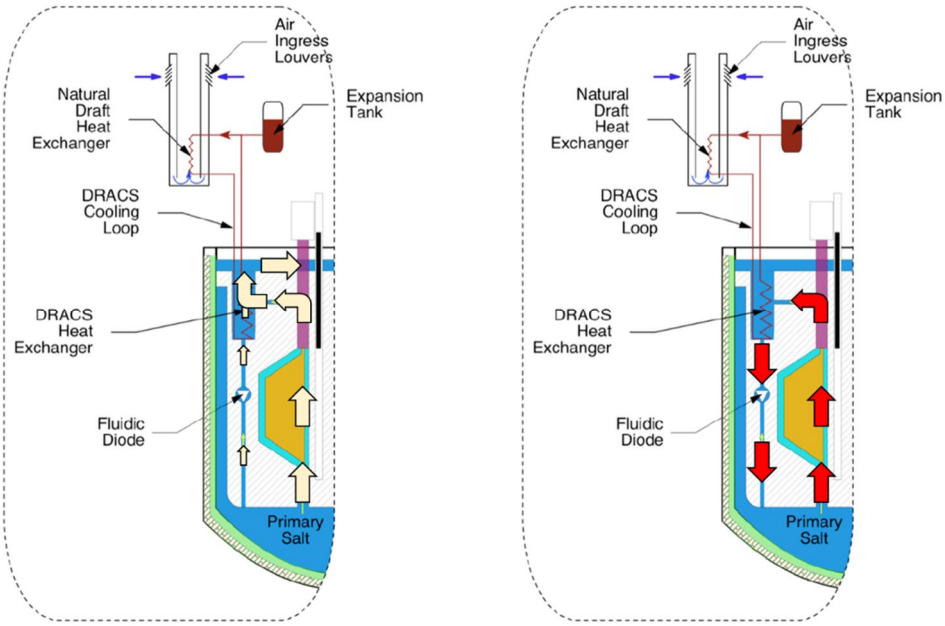

(a) Normal operation (b) Accident condition

Figure 1.2 Flow paths for DRACS facility in FHRs (Holcomb et al., 2009)

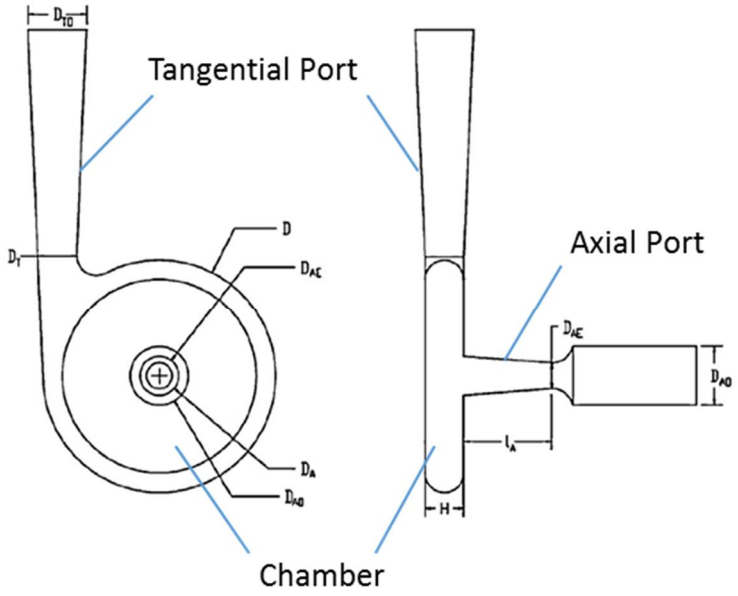

Figure 1.3 Schematic drawing for vortex-type fluidic diode
(Pandare and Ranade, 2015)

(a) Forward flow mode (b) Reverse flow mode

Figure 1.4 Flow configutaion of vortex-type fluidic diode
(Lv, Q, et al., 2013)

Chapter 2

Topology Optimization for Vortex-type Fluidic Diode

2.1 Overview of Topology Optimization

Topology optimization is a one of optimization method to find the optimum material distribution in given design domain. Since it determines the material distribution of all design domain, new design concepts for engineering problem can be obtained through this technique. It has been implemented by finite element methods (FEM), and uses various gradient-based optimization algorithms - SNOPT, method of moving asymptotes (MMA), Levenberg-Marquardt and etc. After first introduction in material science field, its area has been expanded to other research fields such as heat transfer and fluid flow.

Topology optimization for fluid flow is conducted using same basic concepts as other conventional optimization methods, as shown in Table 2.1. The key difference between topology optimization and other conventional optimization is the usage of density function. Density function is a function of the material distribution of the whole design domain, which used as design variable during optimization process. By defining density function on each grid and changing its

value during optimization process, new design concept can be obtained. In principle, density function should have discrete value, 0 for solid and 1 for fluid region. However, it is practically assumed to be a continuous function between 0 to 1 for numerical stability of optimization process with gradient-based algorithm.

2.2 Basic Equations and Algorithm

2.2.1 Fluid Dynamics Equations

In topology optimization for fluid flow, mass and momentum conservation equations are solved to obtain flow variables. In this study, general Navier-Stokes equation with incompressible flow assumption was applied for fluid flow analysis. The equations were applied with some modification as follows.

$$\nabla \cdot \overline{u} = 0 \tag{2.1}$$

$$\rho \frac{\partial \overline{u}}{\partial t} + \rho \left(\overline{u} \cdot \nabla \right) \overline{u} = -\nabla P + \mu \nabla^2 \overline{u} + \overline{f}_d \tag{2.2}$$

where ρ is the density, μ is the viscosity, $\overline{u}$ is the velocity, P is the pressure, and $\overline{f}_d$ is additional Darcy friction force.

Continuity equation for incompressible flow is used as mass conservation equation. In momentum equation, Darcy friction force term is added in the general Navier-Stokes equation to calculate flow field in solid region ($\gamma = 1$) and intermediate region ($0 < \gamma < 1$). The Darcy friction force term applies additional flow resistance proportional to velocity as shown below.

$$\overline{f}_d = -\alpha \overline{u} \tag{2.3}$$

where α is the degree of the impermeability. α is a function of density

function (γ) to vary from lower limit to upper limit depending on density function (γ). Function formulation is as follows.

$$\alpha(\gamma) = \alpha_L + (\alpha_U - \alpha_L)\frac{q(1-\gamma)}{q+\gamma} \tag{2.4}$$

Where α_L is the lower limit of α and α_U is the upper limit of α. q is a parameter to control convexity of function α as shown in Fig 2.1. In practice, the value for α_L is set to zero, and the value for α_U is set to an infinitely large value.

By adding Darcy friction force term, flow variables can be obtained in all region (fluid, solid, and intermediate), because momentum equation changes according to density function value.

In fluid region (γ = 1), α and $\bar{f}_d$ becomes zero, making momentum equation to be same as the general Navier-Stokes equation as shown below.

$$\rho\frac{\partial \overline{u}}{\partial t} + \rho(\overline{u}\cdot\nabla)\overline{u} = -\nabla P + \mu\nabla^2\overline{u} \tag{2.5}$$

In solid region (γ = 0), α becomes infinitely large value, suppressing flow pass through solid region.

$$\overline{u} = 0 \tag{2.6}$$

In intermediate region (0 < γ < 1), α has intermediate value between zero and α_U. Thus, momentum equation with Darcy friction force term was solved. This equation has form of Brinkman equation for flow passing porous media.

$$\rho\frac{\partial \overline{u}}{\partial t} + \rho(\overline{u}\cdot\nabla)\overline{u} = -\nabla P + \mu\nabla^2\overline{u} - \alpha\overline{u} \tag{2.7}$$

2.2.2 Penalization

As mentioned in previous section, the intermediate region, the region whose density function value is between 0 and 1, is allowed in optimization process and flow variables in this region can be obtained using momentum equation for porous media. However, if considerable amount of intermediate region is included in optimization result, the resulting flow field will be different from real one because of additional friction force applied in that region. Thus, it should be excluded during optimization process to improve the quality of optimization result. To do so, forces applied to fluid should be interpolated in terms of density function. Interpolation conducted for this purpose is called penalization. Penalization method shown in Eq. (2.4) and Fig 2.1 is called Brinkman Penalization. The convexity of interpolation function is determined by parameter q. This parameter can be adjusted considering convergence of optimization algorithm.

2.2.3 Constraints

Constraint is the condition which should be satisfied by design and flow variables during optimization process. Generally, it is applied to enhance stability and efficiency of optimization algorithm. In conventional optimization, constraint is applied as equation or range of variables. Also in topology optimization for fluid flow, basically, mass and momentum equations should be satisfied and density function should satisfy the range from 0 to 1. In addition to this, constraints such as limiting the total rate of change for density function or the amount of total density function can be applied according to problem. Constraints

generally used in topology optimization for fluid flow is given in Table 2.2.

2.2.4 Basic Algorithm

The basic algorithm of topology optimization for fluid flow is shown in Fig 2.2. Before performing optimization, design domain is selected and discretization is conducted. Conditions for fluid flow, initial conditions and boundary conditions are applied to design domain and objective function to be minimized is selected. To begin optimization, initial design, initial density function value is selected. With given design, density function, objective function is evaluated using CFD analysis code. COMSOL multiphysics code was used in this study. If the current design does not satisfy convergence criteria, new design is proposed as a result of optimization algorithm. Optimization algorithm work based on sensitivity, which acquired as a result of sensitivity analysis using adjoint method. Whole optimization process is repeated until proposed design satisfies the convergence criteria.

2.3 Vortex-type Fluidic Diode Design

2.3.1 Geometry and Design Domain

In this study, vortex-type fluidic diode design was conducted mainly for the tangential port and chamber. Topology optimization conducted only in low Reynolds laminar regime because Navier-Stokes equation was used as momentum

equation. Since axial-direction flow can be ignored in this flow regime, chamber and tangential port were approximated as two-dimensional (2-D) geometry as shown in Fig 2.3. The chamber was implemented as square shape to give more freedom during optimization process. The tangential port was implemented as straight pipe and the axial port was assumed to be a central hole of chamber. All geometrical parameters were expressed in dimensionless form with respect to tangential port diameter (D) and listed in Table2.3. The aspect ratio of chamber and diameter of axial port was selected according to previous experiment result (Kulkarni et al, 2008). The central hole of the chamber and end of the straight pipe was set to inlet and outlet for fluid flow, according to flow mode.

Square regions in vicinity of inlet and outlet was excluded from design domain for numerical stability of optimization algorithm. As can be seen in Fig 2.4, whole design domain was divided in two sub-domains to reduce design case. Domain 1 contain chamber region and domain 2 contain tangential port and junction with chamber. Geometrical parameters related with design domain also listed in Table 2.3.

2.3.2 Optimization Process and Conditions

Because appropriate geometrical parameters were selected in Section 2.3.1, optimization conducted with various boundary condition, penalization parameter and domain division. Whole geometry was discretized with triangular unstructured grid as shown in Fig 2.5. Grid for boundary layer was not generated because wall boundaries can’t be specified during optimization process. Detailed information of grid is given in Table 2.4.

For flow condition, normal velocity condition was applied in inlet and its value belongs to low-Reynolds laminar regime. The inlet Reynolds number was derived using flow variables in tangential port like below.

$$\mathrm{Re} = \frac{\rho v_t D}{\mu} \tag{2.8}$$

Where v_t is average velocity magnitude in tangential port with diameter D. The inlet Reynolds number was remained constant because inlet Reynolds number had lower effect on the result compared to domain division and penalization parameters.

In forward flow mode, average velocity value applied in axial port was controlled to apply same amount of flow rate in forward flow mode. It was assumed that flow entering axial port has same velocity for all direction.

Optimization conducted in two steps. In first optimization step, only Domain 1 was used as design domain with zero (fluid) initial density function value. Second optimization conducted to all design domain with first optimization result as initial condition in domain 1 and zero initial density function value in for Domain 2.

The inversion of diodicity (Di) was selected as optimization objective function and constraint that limits the density function range between 0 and 1 was applied. Detailed optimization condition and penalization parameters were listed in Table 2.5.

2.3.3 Optimization Results

The optimization results and their performance are summarized in Fig 2.6 and

2.7. Besides the method depicted in Section 2.3.2, many optimization cases with various domain division and penalization parameters were tried. After these various attempts, results with clear boundary and improved performance was selected as optimization result. It can be found that both results have similar design features – circular shape of chamber, obstacle in tangential port, smooth connection between tangential port and chamber.

2.3.4 Preliminary Performance Evaluation

Topology optimization was performed on small scale under low-Reynolds laminar regime, and boundaries of optimization results were not clearly defined. Therefore, 2D CFD laminar flow analysis with actual boundary in real scale and higher Reynolds number condition was performed to confirm that optimization results are still valid in real boundary, laminar flow conditions.

As can be seen in Fig 2.8, topology optimized (T.O) geometry was extracted from optimization results and discretized using triangular unstructured gird. Smoothing for rough boundaries was conducted for feasibility and manufacturability of geometry. tangential port diameter (D) of two-dimensional analysis geometry was set as lab-scale value - 13.5 mm, making whole geometry scaled to 67.5 times larger. To confirm improved performance of the optimization result, reference two-dimensional geometry with circle chamber and straight tangential port was made and discretized in the same way as topology optimized geometry, as shown in Fig 2.9. Grid for wall boundary layer was not generated because analysis conducted using laminar flow model. Information of grid for two-dimensional CFD analysis was listed in Table 2.6.

Two-dimensional CFD analysis was conducted in laminar flow regime, and the inlet Reynolds numbers range from 300 to 2500. Flow boundary conditions were applied in the same manner as described in Section 2.3.2. Detailed information for two-dimensional CFD analysis condition was listed in Table 2.7

Pressure drop characteristic of vortex-type fluidic diode can be expressed using dimensionless Euler number (Eu) and its formulation is like below.

$$Eu = \frac{\Delta P}{\frac{1}{2}\rho v_t^2} \tag{2.9}$$

Where ΔP is pressure drop across the vortex-type fluidic diode.

The diodicity can be express as a ratio of Euler number values in forward flow mode and reverse flow mode. Two-dimensional CFD analysis results were expressed in these variables in Fig 2.10. It was confirmed that performance acquired in topology optimization maintained at same inlet Reynolds number condition, and diodicity increases as inlet Reynolds number increases as shown in Fig 2.10 (c). The diodicity increases because Euler number in reverse flow mode increases with the inlet Reynolds number and Euler number in reverse flow mode decreases. The topology optimized geometry has better performance over all inlet Reynolds number ranges than reference geometry.

2.3.5 Part Design

Three-dimensional topology optimized (T.O) design of vortex-type fluidic diode was designed based on two-dimensional topology optimized geometry in Fig 2.8. The chamber height and the structure of the axial port and tangential port extension were determined with reference to previous study result (Kulkarni et al.,

2008). Chamber height and diameter of axial port has same value with diameter of tangential port (D). Each ports are consisted with straight pipe and diffuser, can be seen in Fig 2.11. Geometrical parameters were expressed as dimensionless form with respect to tangential port diameter and listed in Table 2.8. Entire structure of topology optimized design was shown in Fig 2.12.

Table 2.1 Basic concepts of topology optimization for fluid flow
(Serin Shin et al, 2017)

Concepts	Meanings
Objective function ($\Phi(\gamma, s(\gamma))$)	Variables to be maximize/minimized during optimization process
Design variable (γ)	Variables changed during optimization process which determine geometry design
Flow variable ($s(\gamma)$)	Flow-related variables obtained from CFD analysis from given geometry (γ)
Constraint ($R(\gamma, s(\gamma))$)	Conditions which design and flow variables must satisfy during optimization process
Sensitivity ($\frac{d\Phi}{d\gamma}$)	Rate of change of the objective function w.r.t design variables, which used to find new design variable value during optimization process

Table 2.2 Constraints of topology optimization (Serin Shin et al, 2017)

Constraints	Meaning
$R(\gamma, \mathbf{s}) = 0$	Equations should be satisfied by flow/design variables. (Basically, Fluid dynamic equations)
$0 \leq \gamma \leq 1$	Range of density function value should be limited between 0 and 1
$\sum_{i=1}^{N} \gamma_i \leq V$	A total value of densify function should be less than V (Design domain should have certain portion of solid region)
$\int_{\Omega} \left[\left(\frac{\partial\gamma}{\partial x}\right)^2 + \left(\frac{\partial\gamma}{\partial y}\right)^2\right] d\Omega \leq N$	A total value of density function change should be less than N (Design variable should not have a sudden change in value (e.g. small pockets in solid region))

Table 2.3 Geometrical parameters for 2-D optimization geometry and design domain

Parameters	Values
Tangential port diameter (D)	0.0002 m
Chamber aspect ratio (w/D)	6
Tangential port aspect ratio $((L_{tan} + L_{ent})/\mathrm{D})$	3
Axial port entrance region ratio $(L_{ent,a}/D)$	1.5
Divided domain length ratio in division a $(L_{div,a}/D)$	3
Divided domain length ratio in division b $(L_{div,b}/D)$	2

Table 2.4 Information for gird used in optimization

Domain division	Division a	Division b
Total Number of elements	17151	17089
Minimum element quality	0.743	0.732
Average element quality	0.9859	0.9848

Table 2.5 Optimization conditions and parameters

Category	Classification	Details
Flow Conditions	Inlet Reynolds number	300
	Outlet pressure	0 Pa
Optimization Conditions	Objective function	Inversion of diodicity ($^{1}/_{Di}$)
	Constraint	Density function Constraint ($0 \leq \gamma \leq 1$)
	Penalization parameters	$\alpha_L = 0$
		$\alpha_U = 10^8 \sim 5 \times 10^8$
		$q = 0.1 \sim 0.2$

Table 2.6 Information of gird for 2-D CFD analysis

Geometry	T.O	Reference
Total Number of elements	74233	60386
Minimum element quality	0.1168	0.7343
Average element quality	0.9809	0.9834

Table 2.7 2-D CFD analysis conditions

Classification	Details
Analysis model	Laminar Flow model
Inlet Reynolds number	300, 500, 1000, 2500
Outlet pressure	0 Pa
Wall boundary condition	No-slip condition

Table 2.8 Geometrical parameters for 3-D topology optimized design

Parameters	Value
Chamber height (h/D)	1
Tangential port inner length (L_{tan}/D)	2.08
Tangential port diffuser length ($L_{tan,dif}/D$)	3.12
Tangential port diffuser diameter (D_{tO}/D)	1.636
Axial port length (L_A/D)	2.2
Axial port diffuser diameter (D_{AE}/D)	0.8
Axial port expansion diameter (D_{AO}/D)	1.636
Axial port connection radius (r_{AE}/D)	0.64

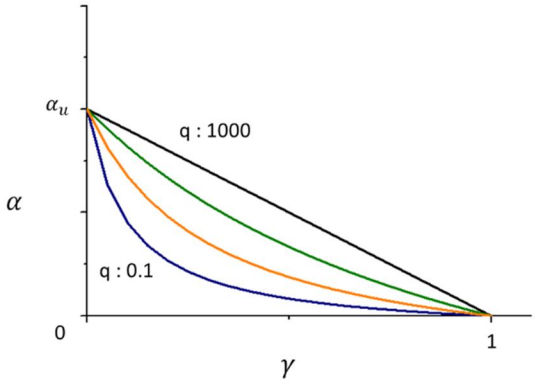

Figure 2.1 Brinkman penalization function

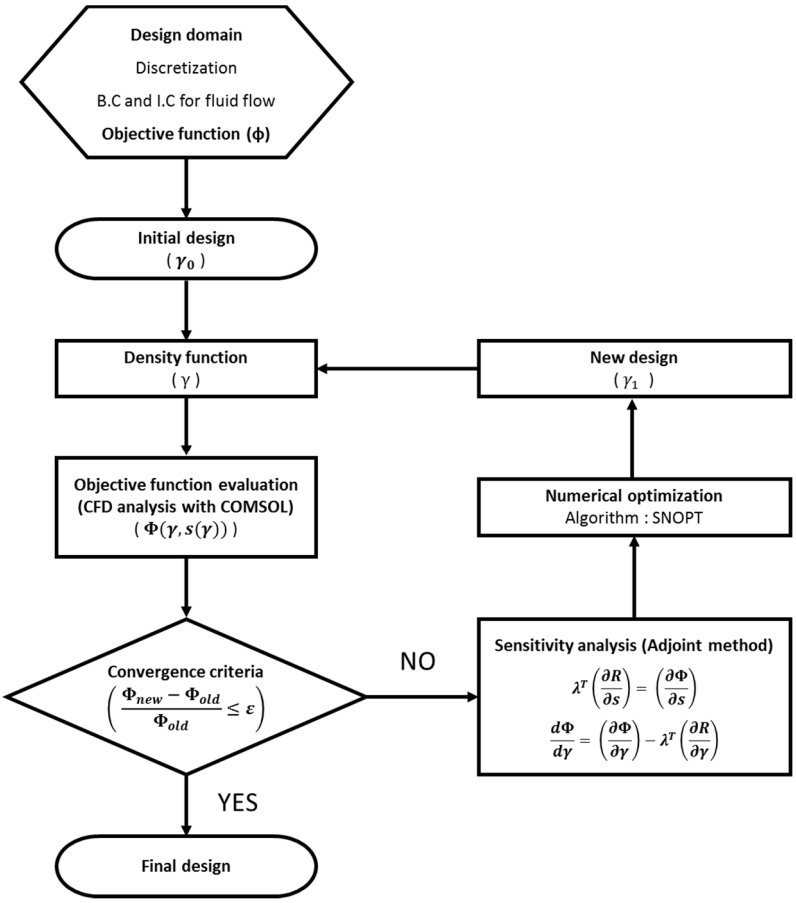

Figure 2.2 Basic algorithm of topology optimization for fluid flow

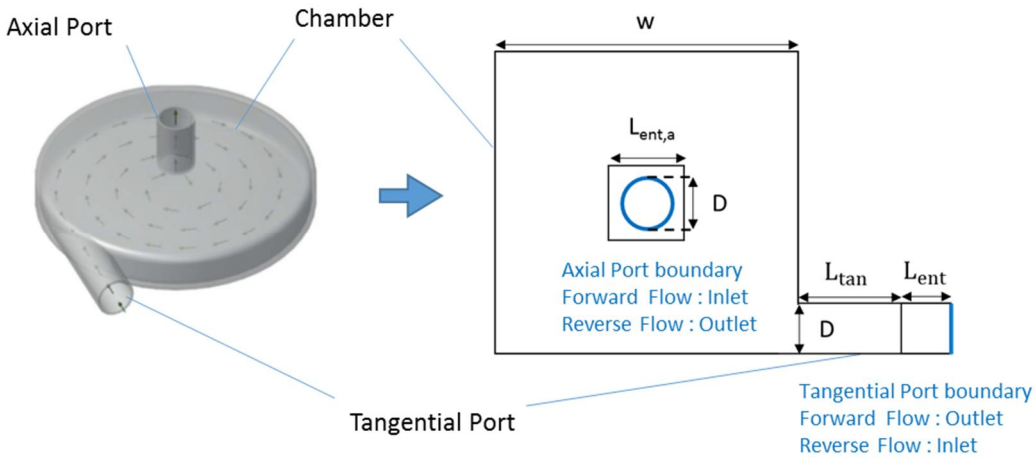

Figure 2.3 2-D optimization geometry and boundary conditions

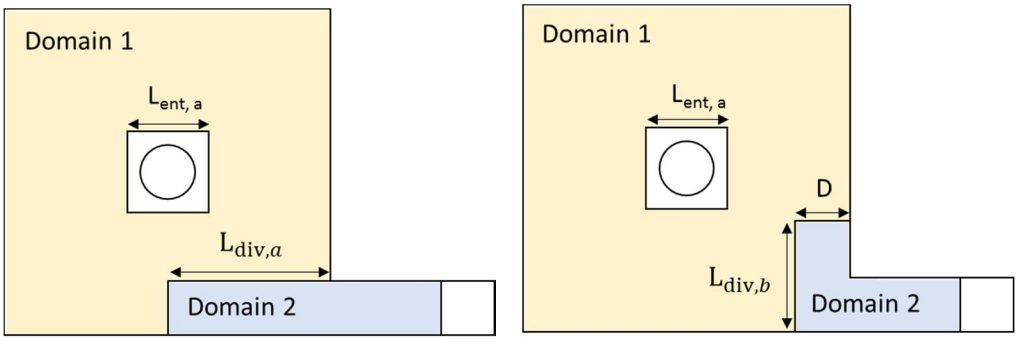

(a) Domain division a (b) Domain division b

Figure 2.4 Divided design domains

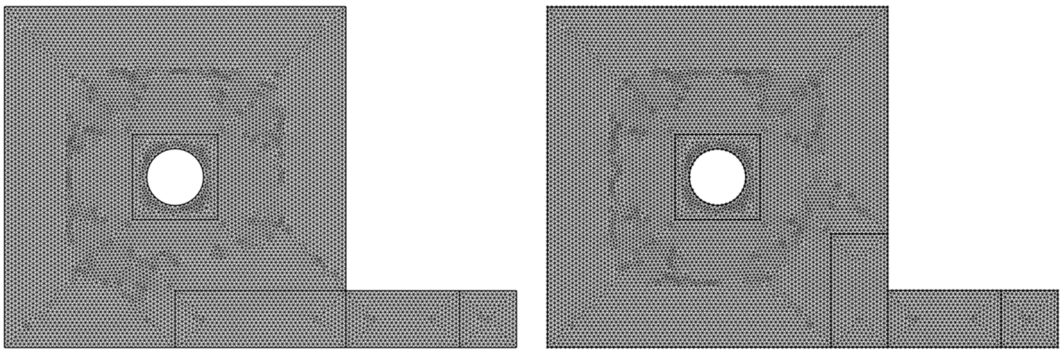

(a) Domain division a (b) Domain division b

Figure 2.5 Grid for optimization geometries

	Division a	Division b
Density function (γ)	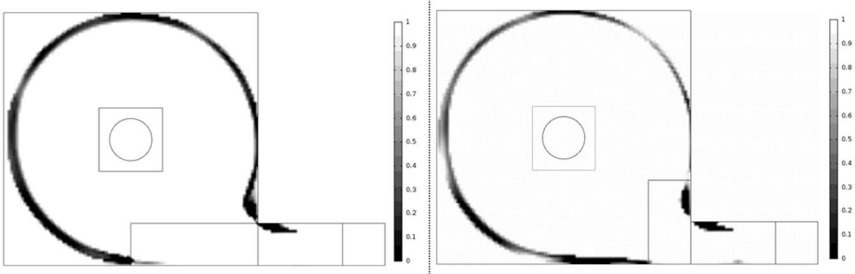	
$\Delta P_{forward}$	2407.9 Pa	2403.4 Pa
$\Delta P_{reverse}$	46345 Pa	51155 Pa
Diodicity (Di)	19.247	21.284

Figure 2.6 Optimization results : density function

	Division a	Division b	Legend
Forward Flow	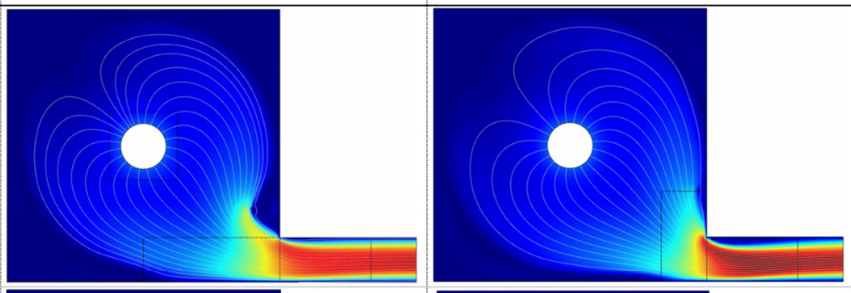		
Reverse Flow	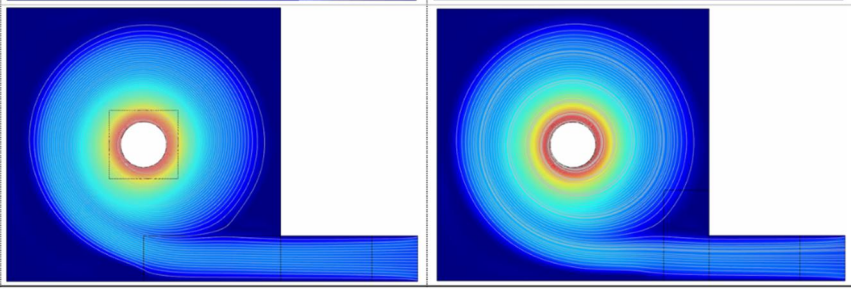		

Figure 2.7 Optimization results : velocity field and streamlines

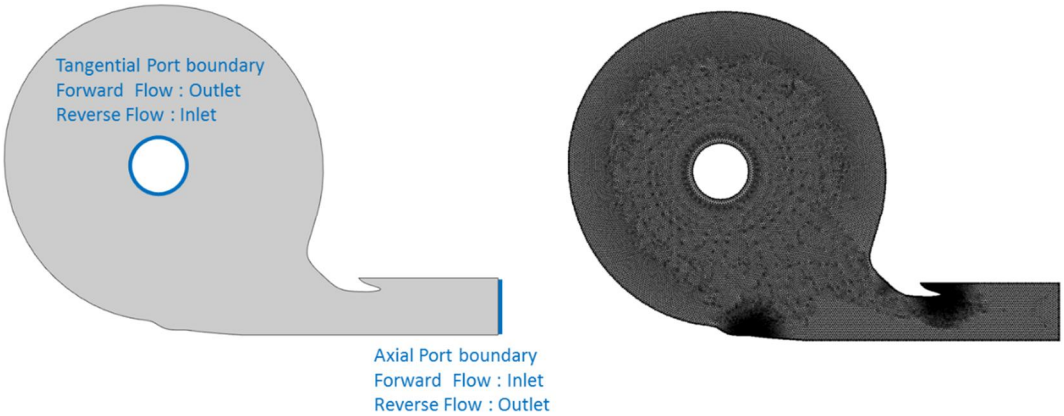

(a) Geometry (b) Grid

Figure 2.8 Geometry and grid for 2-D CFD analysis : T.O geometry

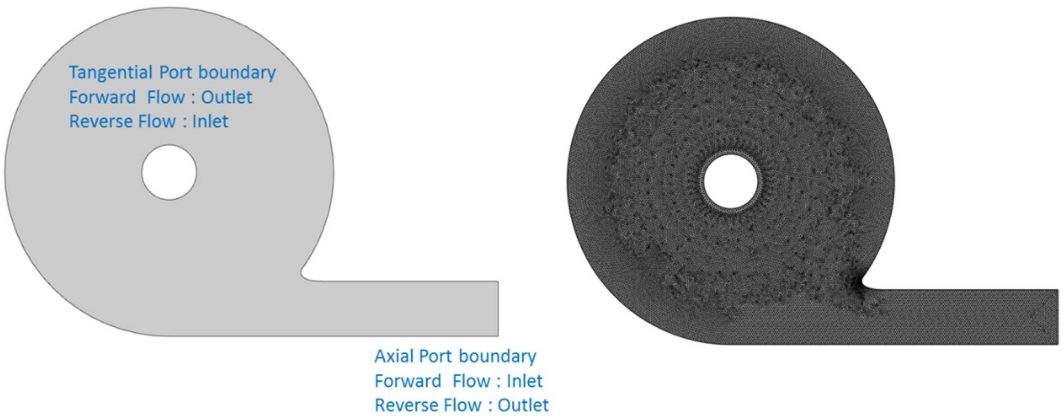

(a) Geometry (b) Grid

Figure 2.9 Geometry and grid for 2-D CFD analysis : reference geometry

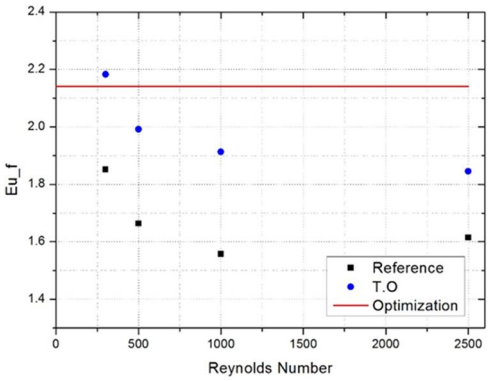

(a) Euler number (Forward)

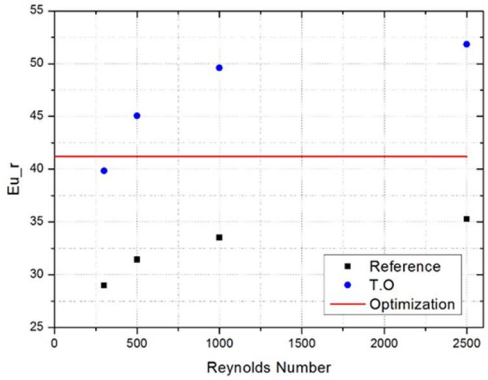

(b) Euler number (Reverse)

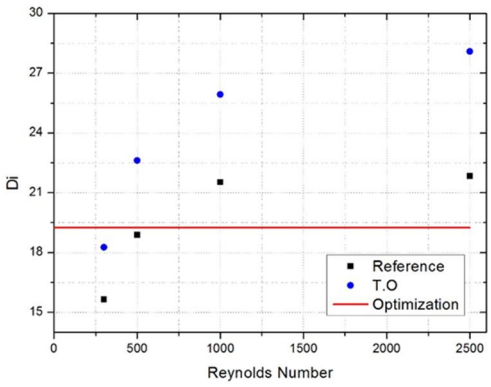

(c) Diodicity

Figure 2.10 2-D CFD analysis Results

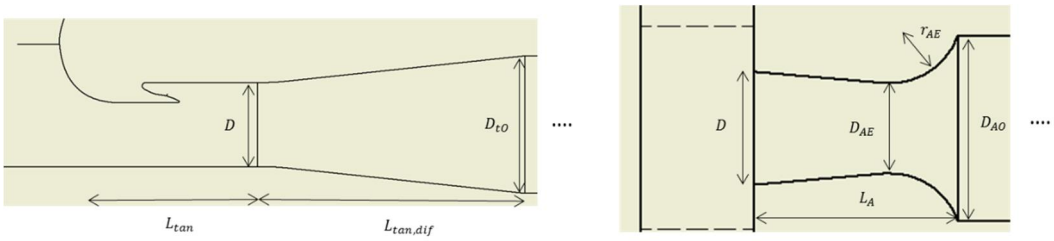

(a) Tangential port (b) Axial port

Figure 2.11 Schematic drawing for tangential and axial port of 3-D T.O design

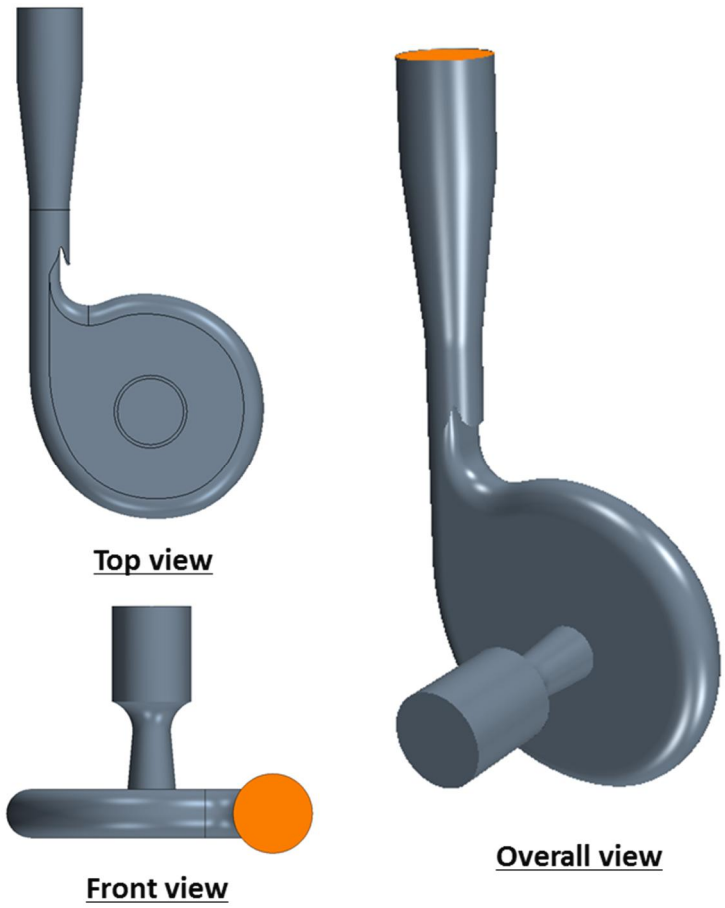

Figure 2.12 Entire structure of 3-D T.O design

Chapter 3

Performance Evaluation using Experimental Study

Topology optimized (T.O) design was acquired as a result of topology optimization and part design process. However, the performance of topology optimized design need to be evaluated because only simple two-dimensional laminar flow analysis was performed. For this reason, pressure drop measurement and flow visualization experiment were conducted to evaluate the performance of topology optimized design.

3.1 Experimental Setup

3.1.1 Test section

Experiment was conducted for two kinds of test section – reference design and topology optimized design. The design proposed in previous study (Kulkarni et al., 2008) was selected as the reference design. The topology optimized design and reference design were compared in Fig 3.1. It can be found that topology optimized design has deformed chamber and additional obstacle in tangential port, compared with reference design.

To make transparent and smooth test section without division or shape

distortion, both types of test sections were produced using Stereolithography(SLA) 3-D printing technique with epoxy resin. The test sections were constructed with 0.5mm thickness layer at an angle of 45 degrees from the axial port to minimize laser reflection due to layer structure. 3D CAD model and photo model for each test sections were shown in Fig 3.2 and 3.3, respectively. Guide plane was added to specify measurement plane. Tangential port diameter (D) of each test section was 13.5mm and thickness of test section wall is 3mm. More detailed geometrical parameters were listed in Table 3.1.

3.1.2 Test Loop

The schematic drawing for test loop was presented in Fig 3.4. The entire loop was designed to conduct flow visualization and pressure drop measurement with special oil for flow visualization in atmospheric pressure condition. Entire loop consists of reservoir, fluid supply pump, pressure transmitter and flow meter. Test section was submerged in the reservoir that also serves as a visualization area. Fluid comes from reservoir is derived by centrifugal pump and pass through test section and exits to reservoir. The reservoir is 2 x 0.4 x 0.6 m square. Flow rate was monitored by two kinds of flowmeter, turbine flowmeter and rotameter. The turbine flowmeter was used in high flow rate condition and the rotameter was used in low flow rate condition. The rotameter was calibrated using a turbine flow meter under high flow rate condition. Differential pressure transmitter was used to measure the pressure drop across the test section. Because the pressure drop across the vortex-type fluidic diode varies greatly depending on the flow mode, pressure drop was also measured using two differential pressure transmitters with

different measurement ranges. In reverse flow mode, one with larger measurement range was used and one with smaller measure measurement range was used in forward flow mode. In case of pressure drop in the reverse flow mode is small enough to measure with differential pressure transmitter of smaller range, pressure drop was measured using the one with smaller range.

The measurement ranges and uncertainty was summarized below. The turbine flowmeter has under ±2% measurement error. The differential pressure transmitter for revers flow mode was ULFA SDTD, which has 0 ~ 3bar measurement range with ±0.25% span error. The other differential pressure transmitter for forward flow mode was SIEMENS SITRNAS P DS Ⅲ, which has 0 ~ 100 mbar range with ±0.075% span error.

3.1.3 Flow Visualization System

In this study, flow inside the vortex-type fluidic diode was visualized using MIR-PIV technique (Song et al., 2015). Special model material and working fluid was selected to enhance quality of data by matching index of refraction (MIR) for specific laser. The model material is TSR-829 and its refractive index for 523nm laser was 1.514. The working fluid is mixture of anise oil and mineral oil. The mixture ratio of oil was controlled to match the refractive index for 523nm laser to 1.514. The ratio was 0.402 and 0.598 for mineral oil and anise oil.

Flow inside the vortex-type fluidic diode was measured using particle image velocimetry (PIV) system of ILA, Germany. This system is consist of 532 nm Nd:Yag laser and CCD camera of 2 megapixel with 14bit range. The camera field of view is 80 x 60 mm and resolution is 1600 x 1200 pixels. Silver-coated hollow

glass spheres having 15μm diameter was selected as seed particles. Application for this system can be seen at Fig 3.5.

The flow visualization was conducted only in reverse flow mode and measurement plane was central region of chamber as depicted in Fig 3.6. Central region of axial port was excluded because vortex flow inside axial port induce out-of-plane error. Images were taken at various time intervals from 50μs to 400μs in order to resolve the strong vortex flow in the chamber. Taken images were filtered before cross-correlation to normalize the brightness of particles. The median, min/max, high pass filter were applied and detailed parameters were listed in Table 3.2.

3.1.4 Flow conditions

Experiment was conducted for two flow mode (forward, reverse) and two types of test section (reference, topology optimized) in same inlet Reynolds number condition, from 2043 to 6128. The inlet Reynolds number was calculated as depicted in Section 2.3.2. Properties of working fluid was acquired from its temperature (20℃). In this temperature, density is 915 kg/m^3 and viscosity is 0.004 kg/m·s. In reverse flow mode of vortex-type fluidic diode, cavitation can be occurred at the central point of chamber when fluid pressure is lower than its vapour pressure due to its high velocity. Thus, the inlet Reynolds number condition was limited to prevent this cavitation phenomenon. The inlet Reynolds numbers and volumetric flow rate correspond to them were listed in Table 3.3.

3.2 Experimental Results

3.2.1 Pressure drop measurement

The pressure drop characteristics and performance of vortex-type fluidic diode were can be expressed by Euler number (Eu), as explained in Section 2.3.4. The result of pressure drop measurement was expressed using Euler number as shown in Fig 3.7. In Fig 3.7 (a), it can be found that the topology optimized design has higher resistance for forward flow mode than reference design. As can be seen in Fig 3.7 (b), Two designs have similar resistance for reverse flow mode. The Euler number for both flow mode converges as Reynold number increases.

Taken these variables together, it can be seen that the diodicity of topology optimized design was lower than one of reference design. This result is different from what was expected from the optimization result in Chapter 2. Therefore, it is necessary to carry out further experimental and numerical study for the reason why such results were obtained.

3.2.2 Flow Visualization

Standard cross-correlation was applied on the images obtained and filtered by the procedure described in Section 3.1.3 and flow fields for the measurement region as shown in Fig 3.8 was acquired. Size of interrogation window and step size was set as 48x48 pixels and 16 pixels, respectively. Flow fields were acquired for all inlet Reynolds conditions and listed in Fig 3.9. It can be found that a strong vortex was generated in both designs and the vortex center was not consistent

with the geometrical center of the chamber. Comparing location of the vortex center, position of topology optimized design was more shifted in outward direction than the reference design.

In order to compare vortex flow precisely, tangential velocity, velocity component perpendicular to the radial direction, was extracted from the measurement line. The measurement line is straight line parallel to the tangential port pass through the vortex center. The measurement lines for each velocity field were also shown in Fig 3.9. In Fig 3.10, tangential velocities in measurement line for both designs were compared in terms of normalized distance from vortex center. It was found that chamber can be divided into two regions where tangential velocity become linearly proportional to the radius and tangential velocity inversely proportional to radius. The first region is called as forced vortex region and the second region is called as free vortex region, according to previous study (Kulkarni et al., 2008). In both designs, tangential velocity of chamber was well divided into free vortex region and forced vortex region, while local peak value was observed at the edge of chamber. The topology optimized design has higher velocity peak value at the edge of chamber in all Reynolds number range, because obstacle in tangential port reduces cross-sectional area of port. It can be expected that the topology optimized design has higher peak velocity near vortex center, considering higher peak velocity value at the edge of chamber. However, both designs have similar velocity peak value near the vortex center except for when the inlet Reynolds number is 2043. This phenomenon means that the effect of velocity change at the chamber edge is reduced as inlet Reynolds number increases. This trend also can be seen from Fig 3.11 which is comparing the normalized tangential velocity for all inlet Reynolds number condition. It was

found that normalized value for peak velocity near the vortex center increases with the inlet Reynolds number.

Table 3.1 Geometrical parameters for test sections

Parameters	Reference design	T.O design
Tangential port inner diameter (D)	13.508 mm	
Test section thickness	3 mm	
Tangential port inner length (L_{tan})	none	23.696 mm
Tangential port diffuser length ($L_{tan,dif}$)	49.096 mm	42.236 mm
Tangential port diffuser inner diameter	28.098 mm	
Tangential port outer length	44.98 mm	29.239 mm
Chamber width (w)	81.046 mm	75.667 mm
Chamber height (h)	13.508 mm	
Axial port diffuser inner diameter (D_{AE})	10.806 mm	
Axial port expansion inner diameter (D_{AO})	22.1 mm	
Axial port connection radius (r_{AE})	8.644 mm	
Axial port diffuser length (L_A)	75.578 mm	74.422 mm
Axial port outer length	75.578 mm	

Table 3.2 Image filter settings

Filter	Kernel size
Median Filter	5x5
Min/Max Filter	11
High Pass Filter	5.0

Table 3.3 Experimental flow conditions

Variables	Values						
Inlet Reynolds number	2043	2724	3405	4086	4767	5448	6128
Volumetric flow rate (LPM)	5.685	7.579	9.474	11.369	13.264	15.159	17.054

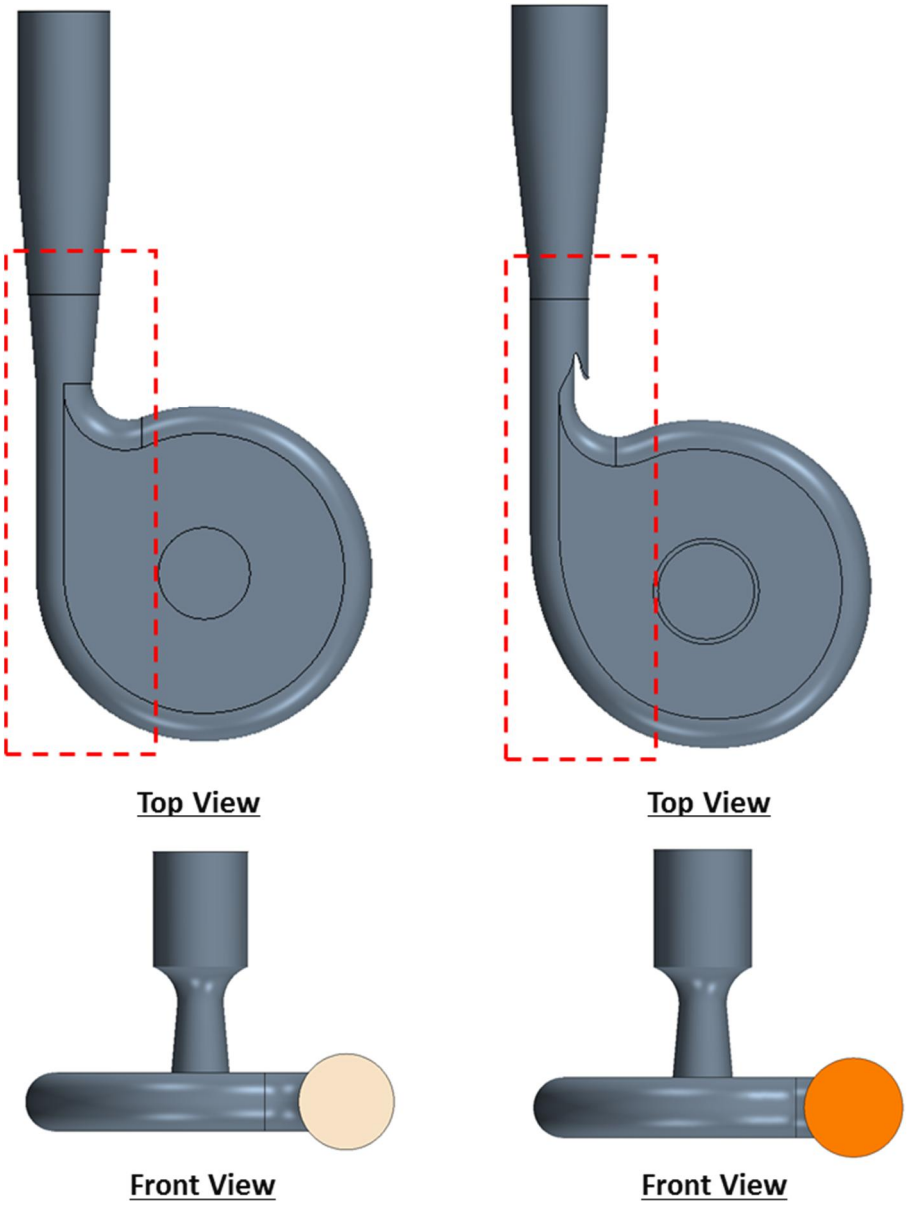

(a) Reference design (b) T.O design

Figure 3.1 Geometry of reference design and T.O design

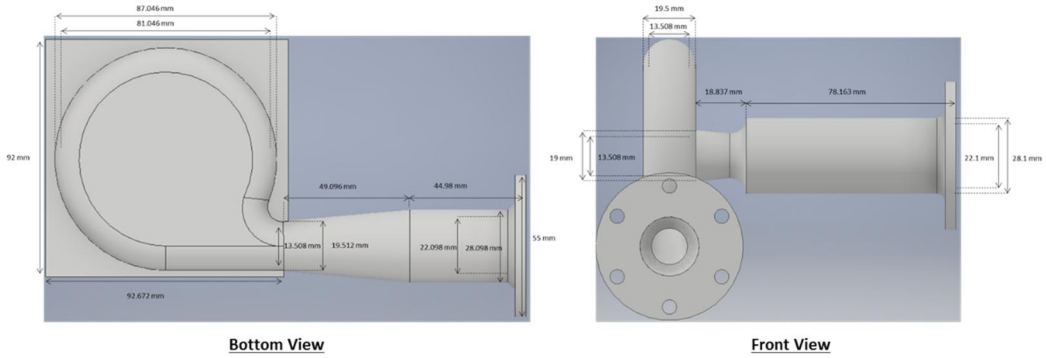

(a) Reference design

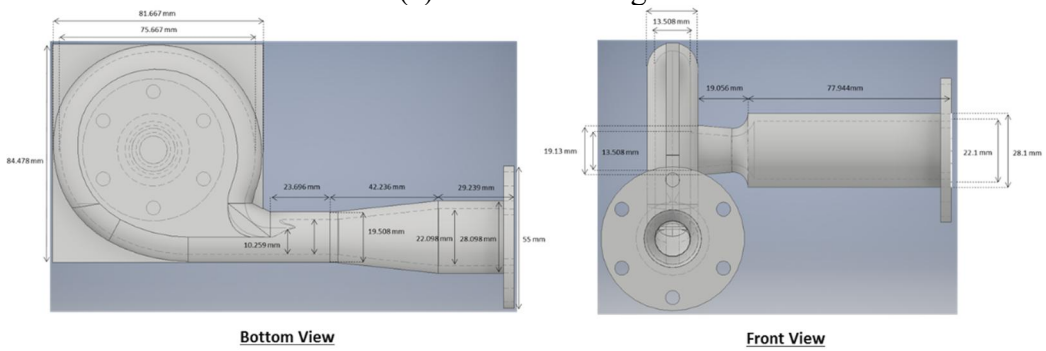

(b) T.O design

Figure 3.2 3-D CAD model for test section

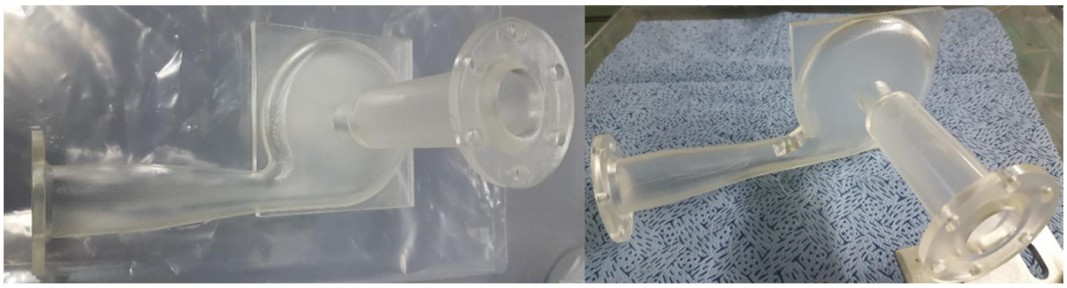

(a) Reference design (b) T.O design

Figure 3.3 Photo of test sections

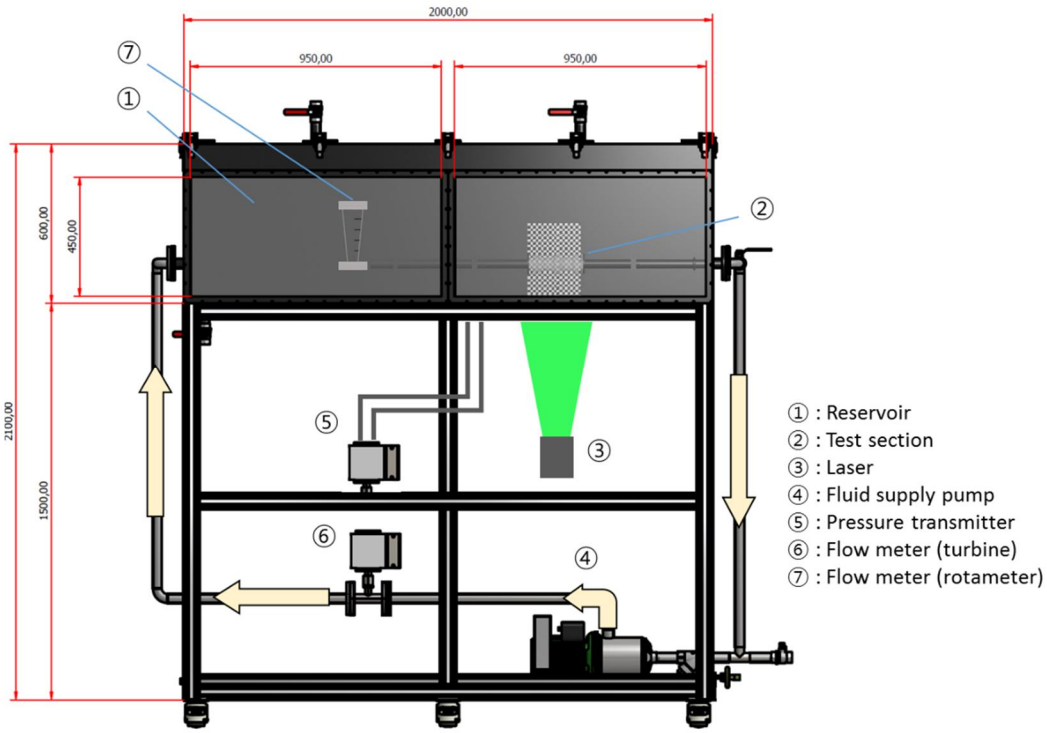

Figure 3.4 Test loop

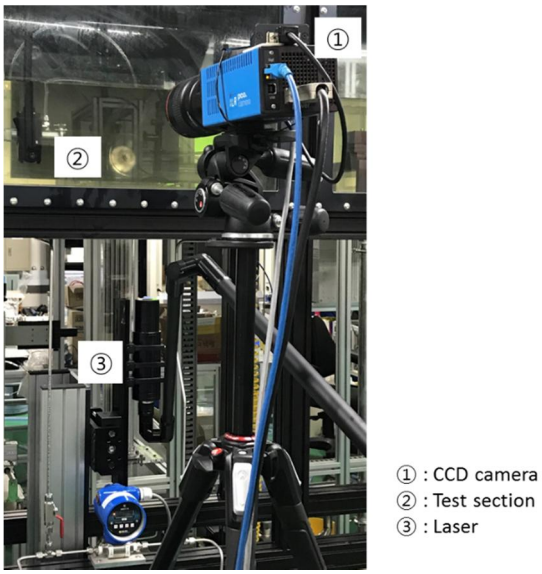

Figure 3.5 Photo of flow visualization system

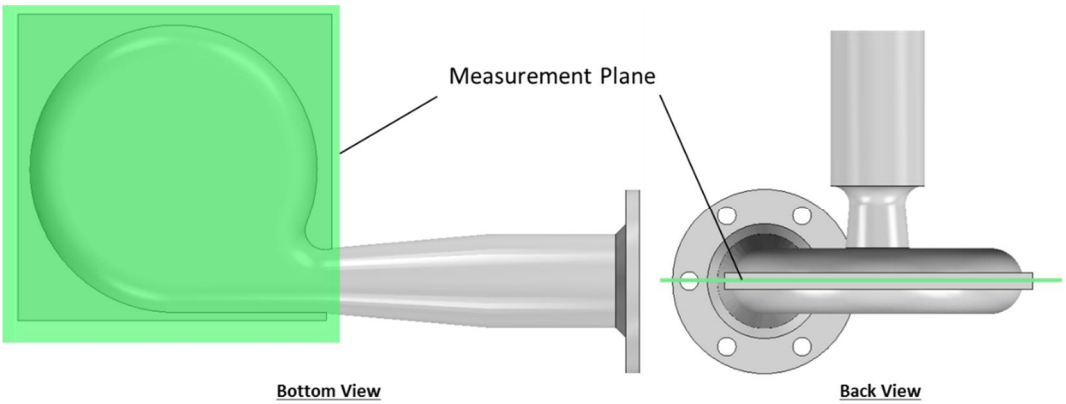

Figure 3.6 Measurement plane for flow visualization

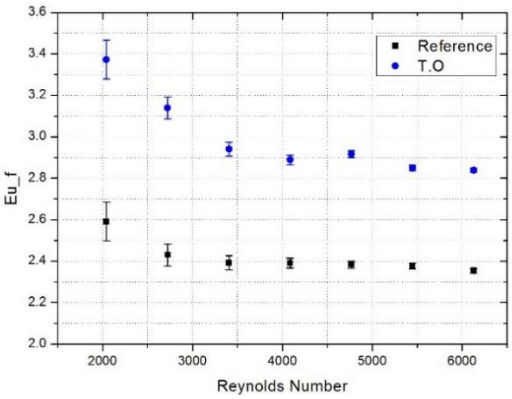

(a) Euler number (Forward)

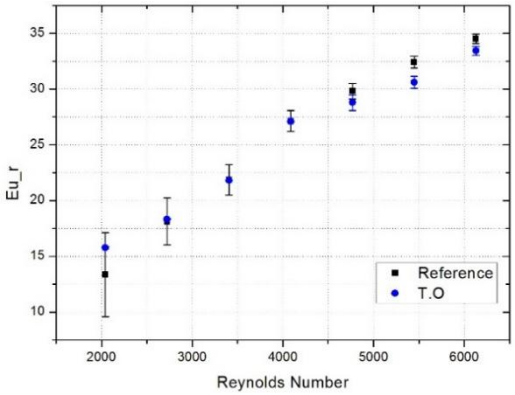

(b) Euler number (Reverse)

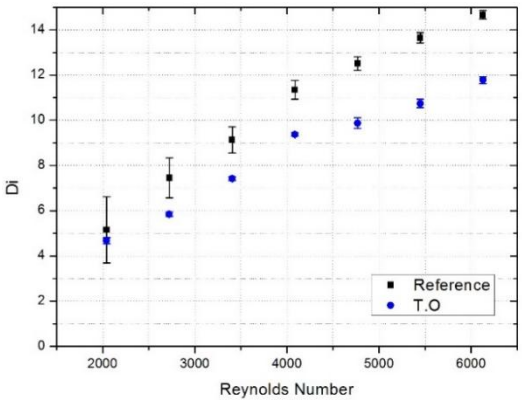

(c) Diodicity

Figure 3.7 Pressure drop measurement experiment results

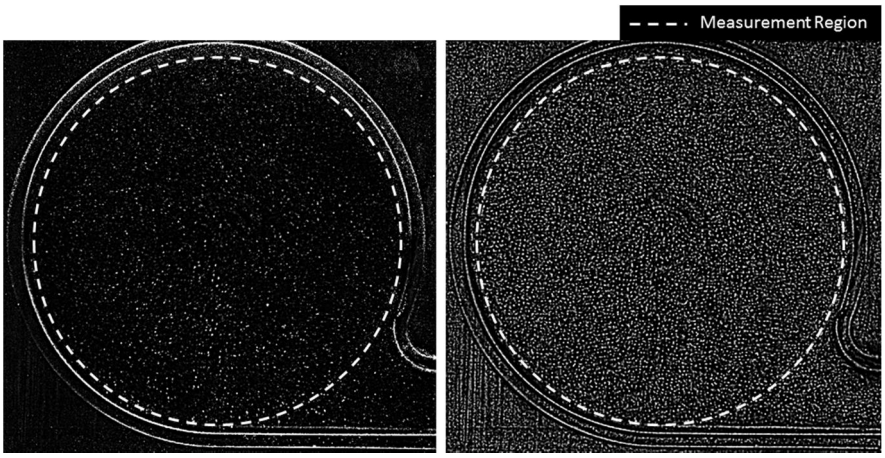

(a) Raw image (b) Filtered image

Figure 3.8 PIV images and measurement region

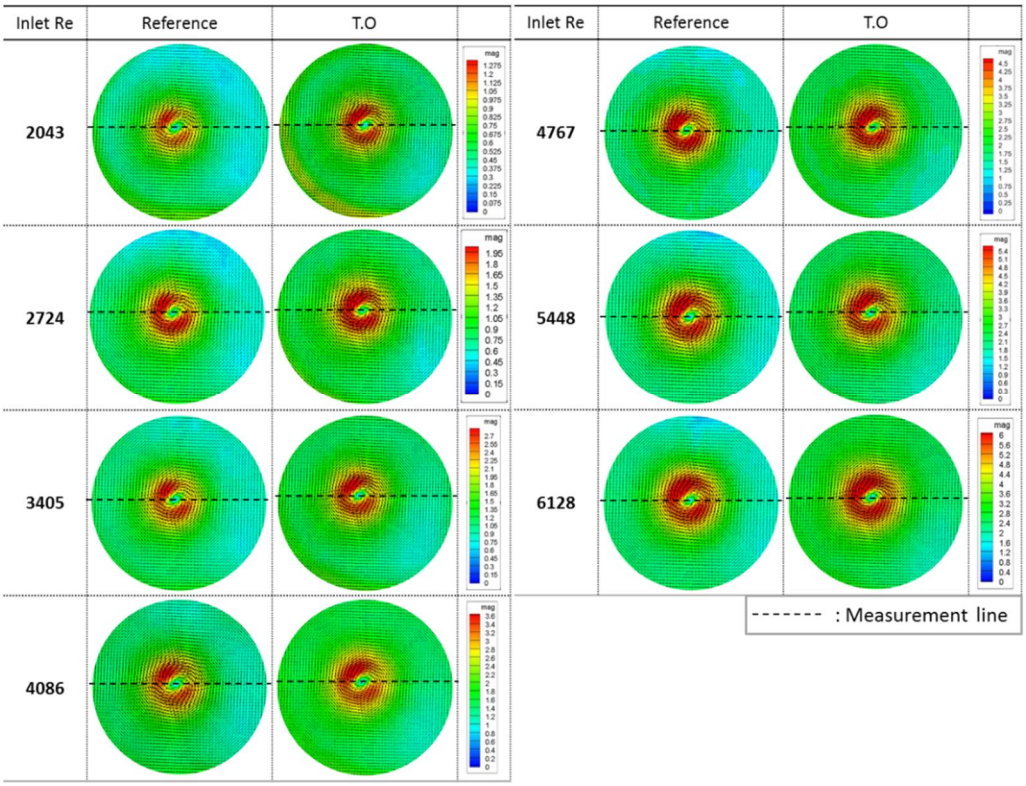

Figure 3.9 The flow fields and measurement lines

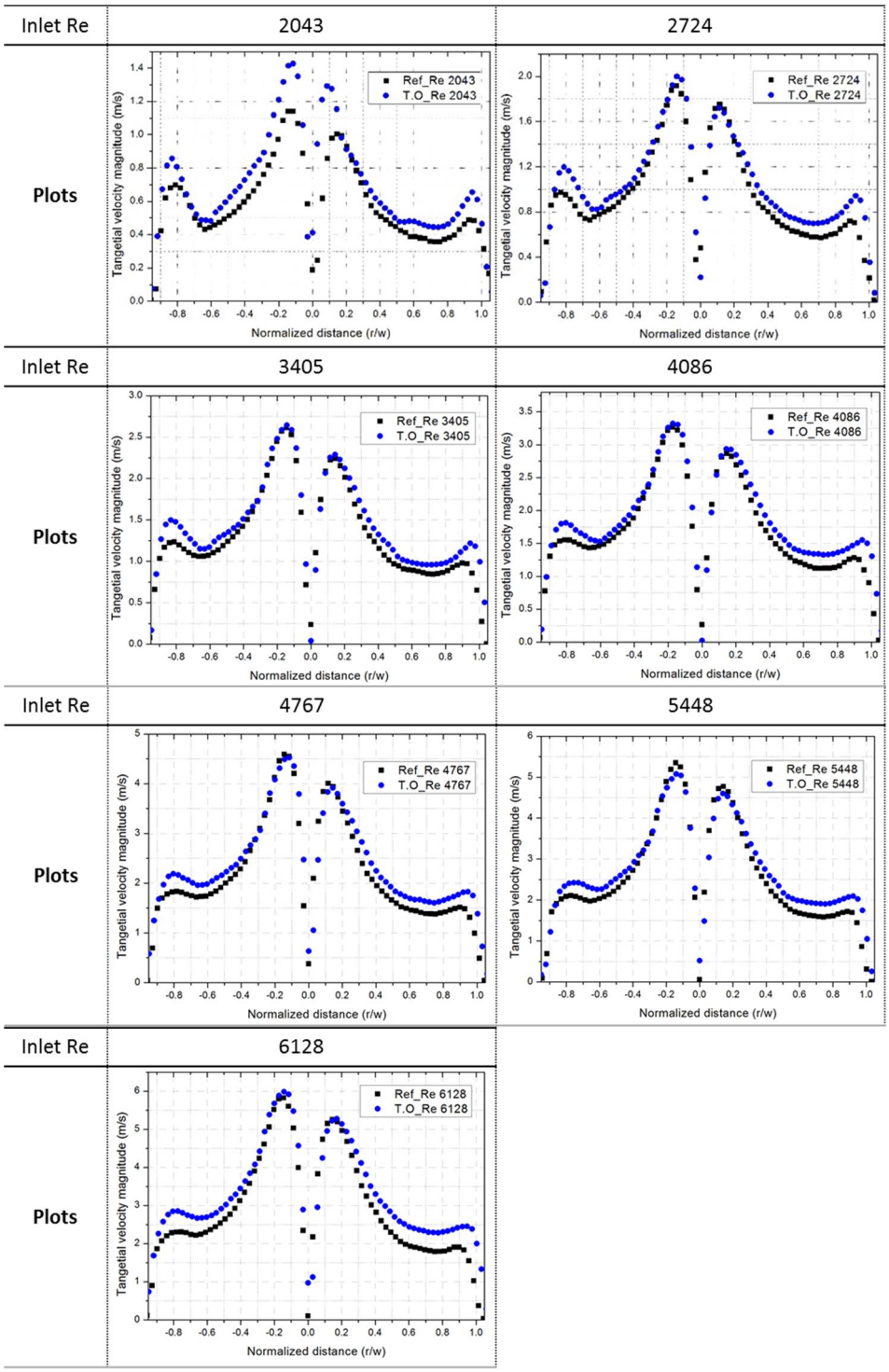

Figure 3.10 Tangential velocity plots in measurement line

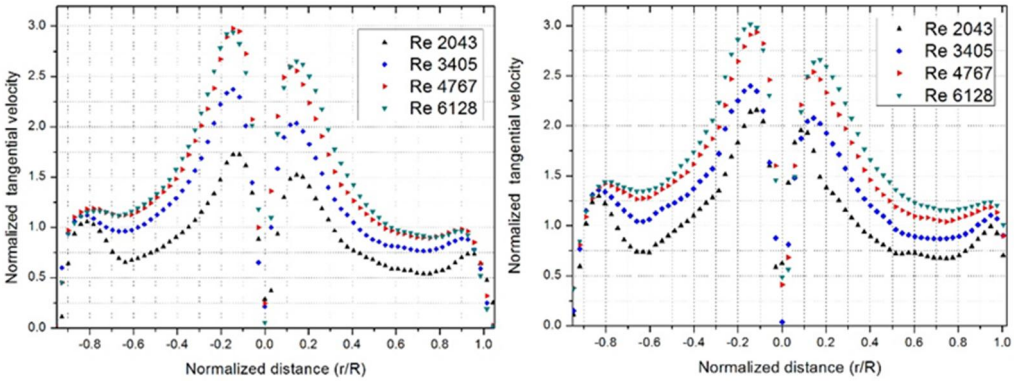

(a) Reference design (b) T.O design

Figure 3.11 Comparison for normalized tangential velocity in measurement line

Chapter 4

Flow Characteristics Investigation using CFD Analysis

In Chapter 3, it was found that topology optimized design has lower performance than reference design, contrary to the results in Chapter 2. Thus, investigation for flow characteristics should be performed in order to know the reason for discrepancy between the optimization results and the experiment results. Detailed three-dimensional (3-D) CFD analysis is an appropriate tool to observe the flow characteristics and pressure changes inside the vortex-type fluidic diode. Therefore, CFD analysis with specialized CFD software was performed on purpose of understanding flow characteristic inside the vortex-type fluidic diode and evaluating the effect of each sub-part on pressure drop.

4.1 Analysis Model and Conditions

4.1.1 Geometry and Grid

3-D CFD analysis was conducted for reference design and topology optimized

design with the same size as described in Chapter 3. In 3-D analysis domain in Fig 4.1, the axial port and the tangential port outer length were extended to provide entrance length in inlet and prevent reverse flow in outlet. The value is about 10D for axial port and about 6D for tangential port.

Grid generation was conducted using internal grid generation program of specialized CFD software, STAR-CCM+. Unstructured grid with polyhedral elements were generated and prism layer was generated near the wall for turbulent flow analysis. Thickness of near-wall mesh was controlled to make y+ value of near wall less than 1.5 in all analysis condition. The grid is shown in Fig 4.2 and detailed information is listed in Table 4.1

4.1.2 Models and Conditions

The flow pattern inside the vortex-type fluidic diode changes as passing through each sub-part. Thus, it is difficult to judge whether the flow inside the vortex-type fluidic diode is in laminar regime or turbulent regime from the inlet Reynolds number. For this reason, in this study, the CFD analysis was conducted using laminar flow model and turbulence model. The CFD analysis was conducted with specialized CFD software, STAR-CCM+.

Among the turbulence model, SST k-w model was selected considering computational cost and accuracy. In general, Reynolds Stress Model (RSM), which directly solves Reynolds stress term has better accuracy than RANS model, which uses eddy viscosity formulation. However, the RSM is highly computationally intensive compared to the RANS model. Therefore, the SST k-w model, which has better accuracy than other RANS models as shown in Fig 4.3,

was selected as turbulence analysis model (Pandare and Ranade, 2015). Default wall function and all y+ treatment were used with turbulence model.

Whole CFD analysis were conducted in the same condition as the experiment. The oil mixture used in experiment in Chapter 3 was assumed as working fluid and its material property at $20°C$ explained in Section 3.1.4 was applied. No-slip boundary condition was applied for wall. For inlet boundary condition, mass flow rate condition was applied and turbulent parameters were applied like below.

$$l_T = 0.07 \times D \tag{4.1}$$

$$I = 0.16 \times (\mathrm{Re})^{-1/8} \tag{4.2}$$

Where l_T is turbulence length scale and I is turbulence intensity.

The pressure outlet condition with 0 Pa was applied for outlet. If only this condition is applied in reverse flow mode, the circulatory flow generated in the chamber is maintained until the outlet then distribution of pressure, which causes the reverse flow from the outlet occurs. To avoid reverse flow from outlet, special loss coefficient was applied as suggested in previous study (Kulkarni, 2008). It was reported that predicted pressure drop result is insensitive to loss coefficient value. The loss coefficient value was gradually increased until there is no reverse flow from outlet. The whole analysis was carried out with unsteady solver. The simulation time steps changes according to inlet boundary condition from 1×10^{-3}s to 1×10^{-4}s and 10 iterations was performed per time step. The convergence of the analysis was determined by the mass flow-averaged pressure value over time at inlet and outlet. Detailed combination of analysis model and inlet boundary condition was listed in Table 4.2. The analysis with laminar model in inlet Reynolds 6128 condition excluded because of its bad convergence.

4.2 Results

4.2.1 Comparison with Experimental Results

The 3-D CFD analysis results were compared to experimental results as shown in from Fig 4.4 to Fig 4.7. The Euler number and diodicity were compared in Fig 4.4 and Fig 4.5. CFD analysis results with SST k-w model were plotted with blue color half-filled rectangles and results with laminar model were plotted with green color half-filled circles. Both models overestimate the pressure drop of the forward and reverse flow modes, and it can be found that the error decrease with increasing inlet Reynolds number. SST k-w model predicts the pressure drop for reverse flow mode more accurately than laminar flow model, and overestimates pressure drop for forward flow mode than laminar flow model. Comprehensively, SST k-w model predicts didodicity more accurately than laminar model for both designs.

The tangential velocity fields in reversed flow mode extracted from the measurement line parallel to the tangential port pass through the vortex center were compared in Fig 4.6 and Fig 4.7. Velocity fields of SST k-w model were plotted with navy colored dash line and velocity fields of laminar model were plotted with blue colored dash-dot line. Both models over estimates the tangential velocity. At the vortex center, laminar model overestimates velocity more than SST k-w model. It was confirmed that SST k-w model predicts tangential velocity more accurately than laminar model for both designs.

From the comparison with the experiment, it is confirmed that the SST k-w model is more suitable for vortex-type fluidic diode analysis under this conditions.

Therefore, in the next section, the results obtained from SST k-w model was used for discussion.

4.2.2 Evaluation of Effect of Sub-part on Pressure Drop

Fluid pass through the vortex-type fluidic diode experience various phenomenon. In forward flow mode, fluid comes from axial port collides with the chamber wall and radially dispersed throughout the chamber. Then the dispersed fluid creates circulator flow at the edge of chamber and finally flow towards tangential port, as depicted in Fig 4.8 (a). In reverse flow mode, fluid comes from tangential port generates vortex and escapes through axial port with maintaining swirl flow, as shown in Fig 4.8 (b).

Since the flow pattern inside the vortex-type fluidic diode changes continuously as fluid pass through each sub-parts, it can be expected that the effect of each sub-part on the pressure drop is different. Therefore, total pressure along a hypothetical line depicted in Fig 4.9 was plotted to observe effect of sub-part on pressure drop. The total pressure distribution along hypothetical line was plotted in Fig 4.10. It can be found that both design has similar total pressure distribution although there is a difference in absolute value. In forward flow mode, significant loss occurs when fluid comes from axial port collide with chamber wall then moderate loss occurs pass through chamber periphery and tangential port. In reverse flow mode, moderate loss occurs when it creates vortex in chamber periphery. Then significant loss occurs when vortex flow suffer transition to axial flow in chamber center and junction with axial port. It was confirmed that for all designs and flow modes, major loss of kinetic energy occurs in chamber

center and junction with axial port.

To compare effect of sub-part on pressure drop in quantitative manner, total pressure changes between hypothetical points in Fig 4.9 were measured. The total pressure changes were normalized to the whole total pressure change and plotted in Fig 4.10. In forward flow mode, major portion of hydraulic loss occurs between P1 and P2 which correspond to the center of the chamber and junction with axial port.

The percentage of losses occurring in this sub-part is up to 75% for reference design and up to 60% for topology optimized design. Moderate portion of hydraulic loss occurs between T and P2 which correspond to tangential port and chamber periphery. In reverse flow mode, major portion of hydraulic loss occurs between P2 and P1 which correspond to the center of the chamber and junction with axial port. The percentage of losses occurring in this sub-part is up to 83% for reference design and 78% for topology optimized design. The hydraulic loss between T and P3 which correspond to tangential port and loss between P1 and A which correspond to axial port are negligible.

In Chapter 3, it was found that topology optimized design has higher pressure drop than reference design, while has similar pressure drop in reverse flow mode with reference design. To confirm how the topology optimized design affected the pressure drop, total pressure changes of reference design and topology optimized design were compared in Table 4.3 and 4.4. The total pressure changes in forward flow mode were compared in Table 4.3 and total pressure changes in reverse flow mode were compared in Table 4.4. It was found that pressure drop between T and P2 increase in topology optimized design in forward flow mode, while pressure drop increases in all sub-parts except for region between P2 and P1 in reverse

flow mode. In general, additional obstacle in fluidic diode enhance its didodicity by further increasing the pressure drop in the reverse flow mode than forward flow mode. Based on the result that total pressure change between T and P1 increase more in reverse flow mode, it can be seen that design modification of topology optimized design functions as intended in topology optimization process. However, considering the contribution of tangential port in both flow mode, design modification effect in forward flow mode maintained because of tangential port's moderate distribution, whereas design modification effect in reverse flow mode becomes insignificant because of tangential port's negligible contribution.

Therefore, it can be concluded that the discrepancy between the optimization results and the experiment results occurs because the degree of contribution of each sub-part was misjudged in the optimization process. This misjudgment was caused since the axial port and chamber center which have most contribution on pressure drop was excluded in optimization process.

Table 4.1 Grid information

Design	Reference	Topology optimized
Total number of elements	1,116,761	1,205,076
Maximum skewness angle	84.85 deg	86.83 deg
Minimum volume change	0.01	0.0016
First near-wall mesh thickness	10^{-5} m	

Table 4.2 Combination of turbulence model and inlet boundary condition

Turbulence model	Laminar	SST k-w
Inlet Reynolds number	2043	2043
	4086	4086
	x	6128

Table 4.3 Total pressure change in forward flow mode

Re		T - P3	P3 – P2	P2 – P1	P1 - T
2043	Reference	96.055 Pa	61.557 Pa	415.081 Pa	9.477 Pa
	T.O	160.875 Pa	96.507 Pa	401.963 Pa	9.458 Pa
	Ratio	1.675	1.568	0.967	0.998
4086	Reference	354.486 Pa	199.871 Pa	1160.79 Pa	21.869 Pa
	T.O	556.366 Pa	429.064 Pa	1542.47 Pa	12.711 Pa
	Ratio	1.569	2.147	0.929	0.581
6128	Reference	717.773 Pa	588.944 Pa	3316.21 Pa	30.164 Pa
	T.O	1343.49 Pa	785.253 Pa	3245.86 Pa	30.024 Pa
	Ratio	1.872	1.33	0.979	0.995

Table 4.4 Total pressure change in reverse flow mode

Re		T - P3	P3 – P2	P2 – P1	P1 - T
2043	Reference	26.965 Pa	673.078Pa	3485.81 Pa	196.39 Pa
	T.O	63.505 Pa	877.809 Pa	3281.99 Pa	281.874 Pa
	Ratio	2.355	1.304	0.942	1.435
4086	Reference	66.690 Pa	3528.14 Pa	19993.5 Pa	823.582 Pa
	T.O	182.70 Pa	4415.51 Pa	18689.1 Pa	1314.02 Pa
	Ratio	2.740	1.252	0.935	1.595
6128	Reference	79.74 Pa	8992.53 Pa	53469.9 Pa	1873.91 Pa
	T.O	356.53 Pa	10624.7 Pa	49743.1 Pa	2977.54 Pa
	Ratio	4.471	1.182	0.930	1.589

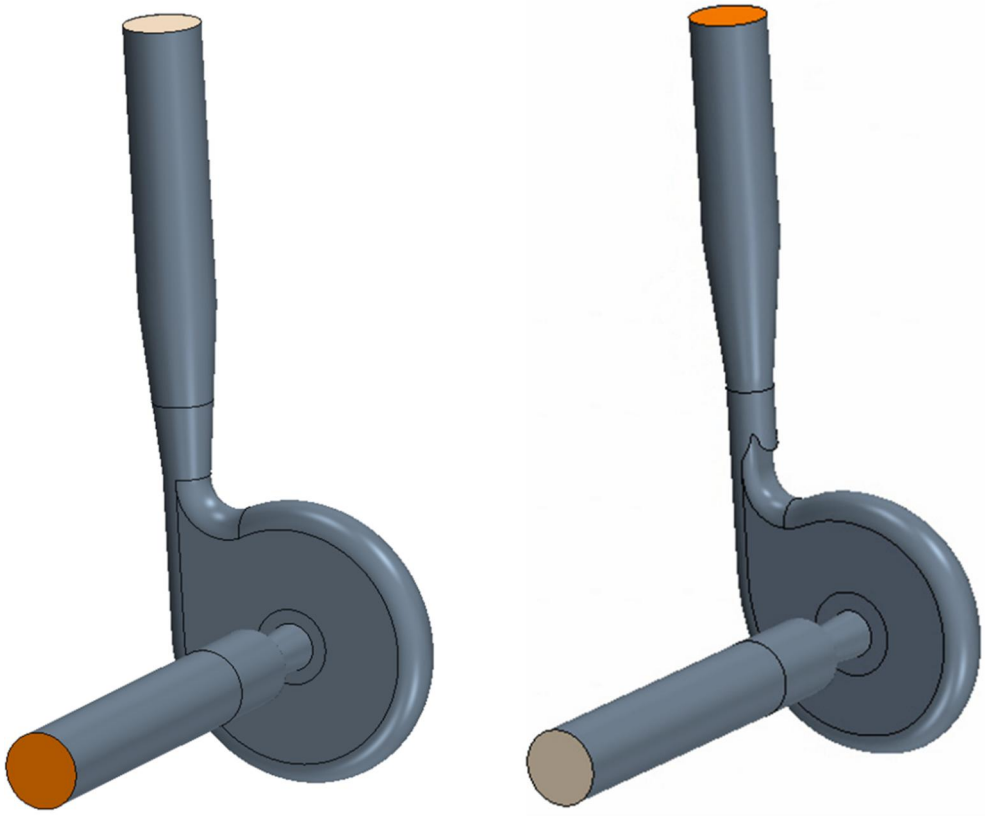

(a) Reference Design (b) T.O Design

Figure 4.1 3-D CFD Analysis domain

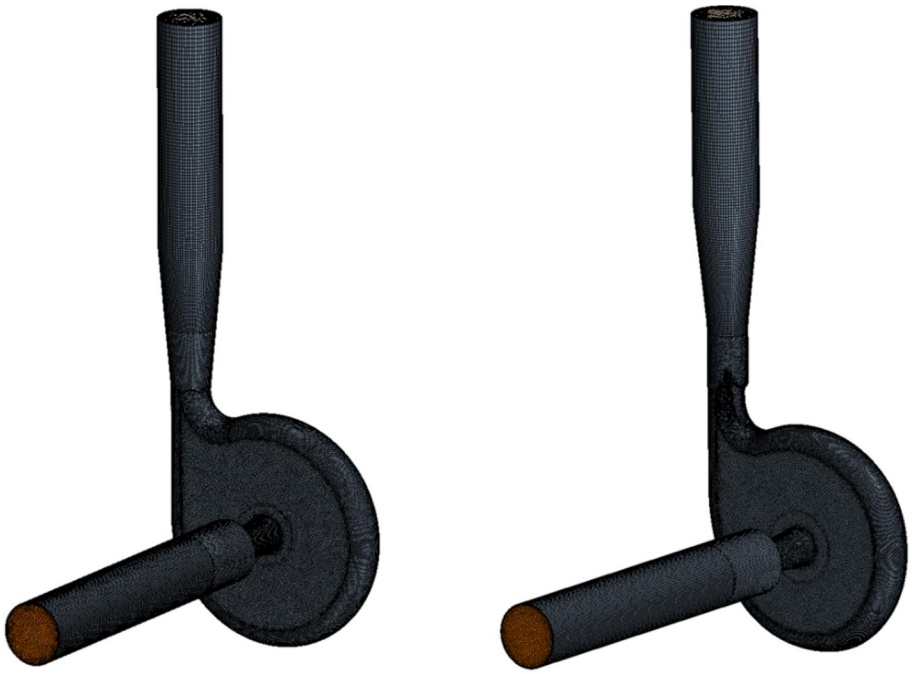

(a) Reference Design (b) T.O Design

Figure 4.2 Grid for 3-D CFD analysis domain

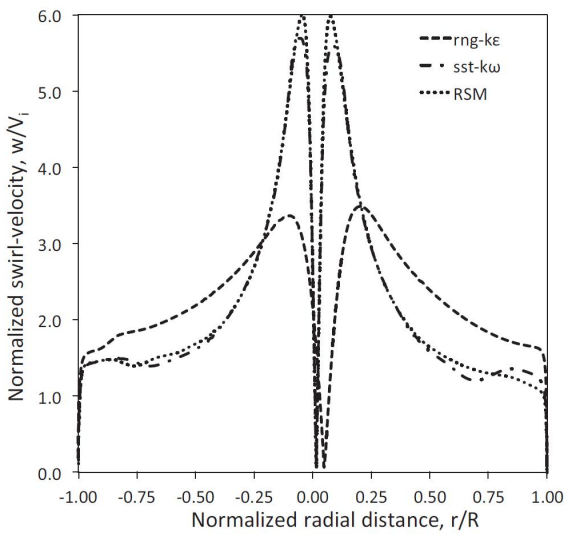

Figure 4.3 Comparison of RANS model to RSM model (Pandare and Ranade, 2015)

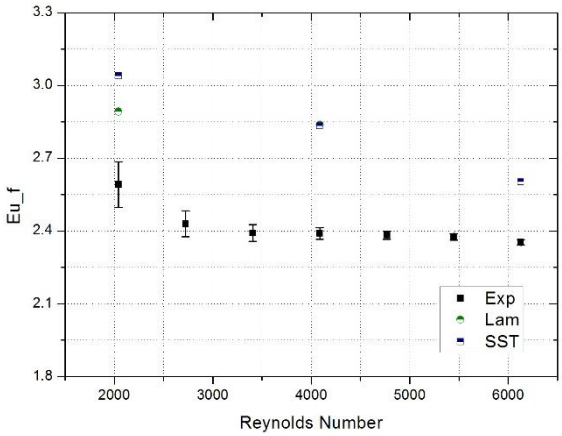

(a) Euler number (Forward)

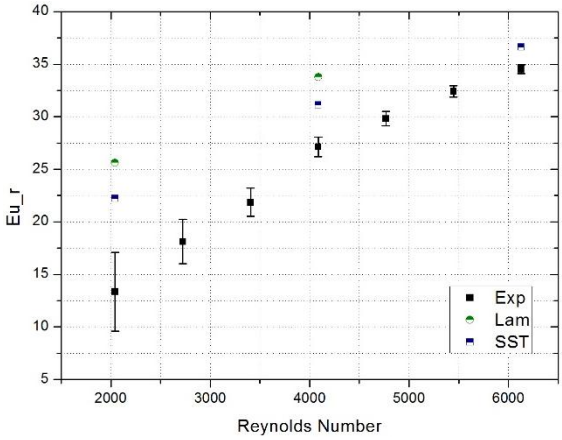

(b) Euler number (Reverse)

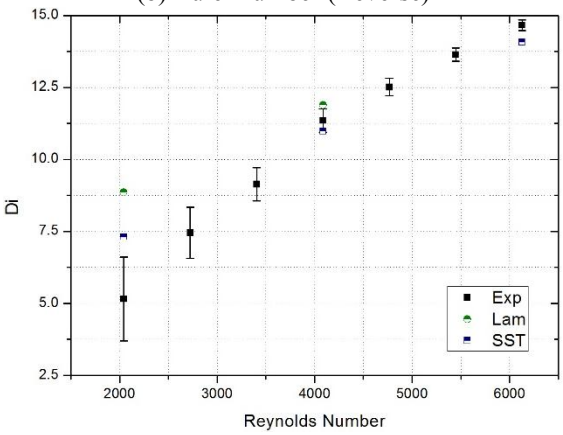

(c) Diodicity

Figure 4.4 Pressure drop comparison between experiments and CFD analysis : reference design

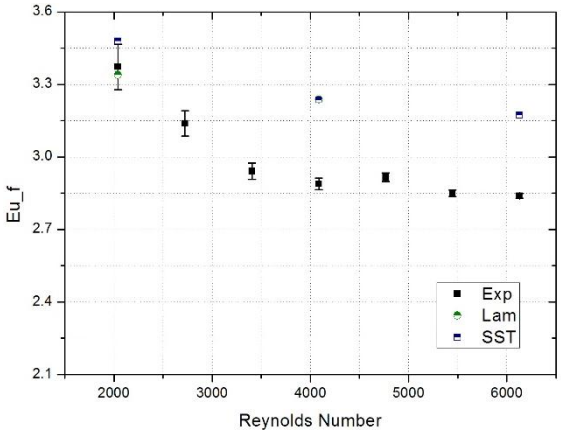

(a) Euler number (Forward)

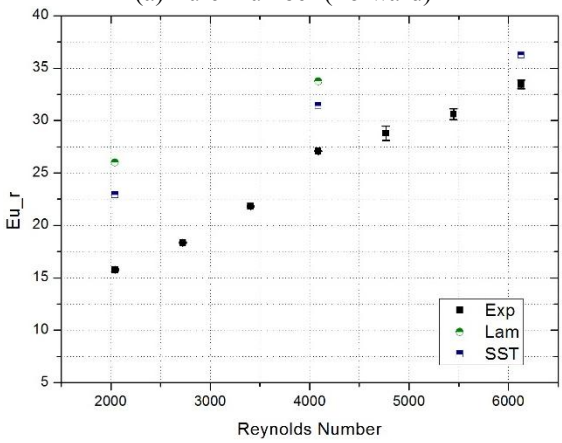

(b) Euler number (Reverse)

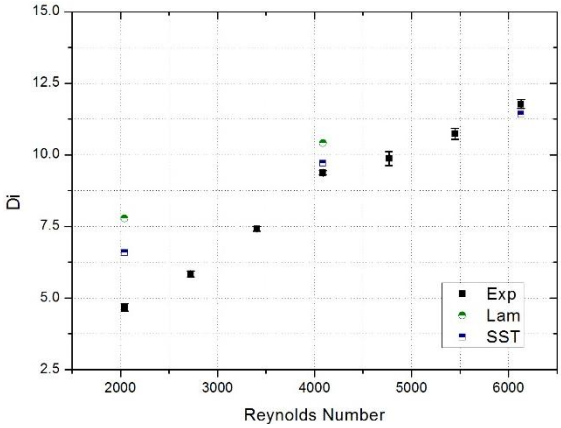

(c) Diodicity

Figure 4.5 Pressure drop comparison between experiments and CFD analysis : T.O design

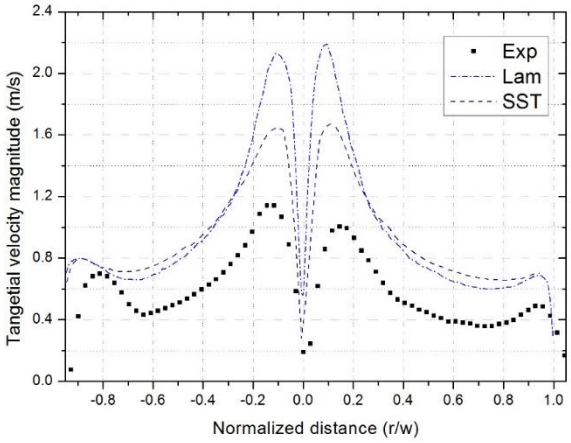

(a) Inlet Re : 2043

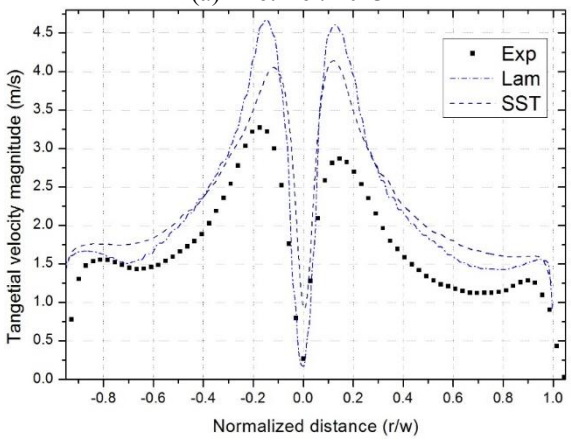

(b) Inlet Re : 4086

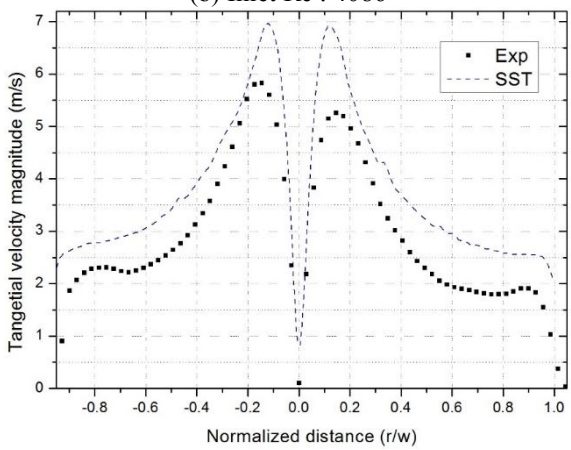

(c) Inlet Re : 6128

Figure 4.6 Chamber tangential velocity field comparison between experiments and CFD analysis : Reference design

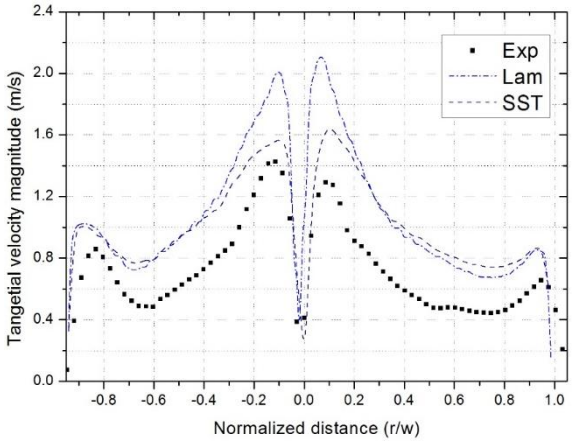

(a) Inlet Re : 2043

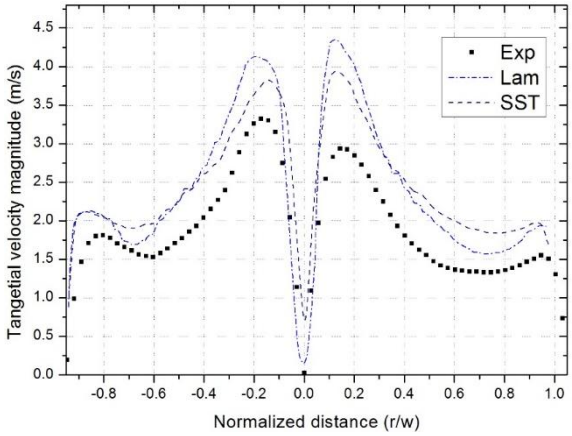

(b) Inlet Re : 4086

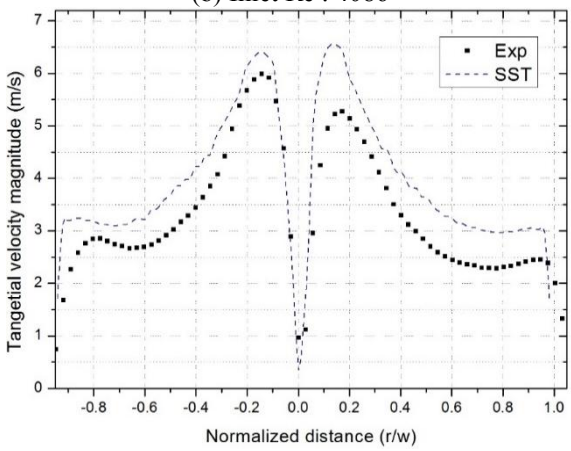

(c) Inlet Re : 6128

Figure 4.7 Chamber tangential velocity field comparison between experiments and CFD analysis : T.O design

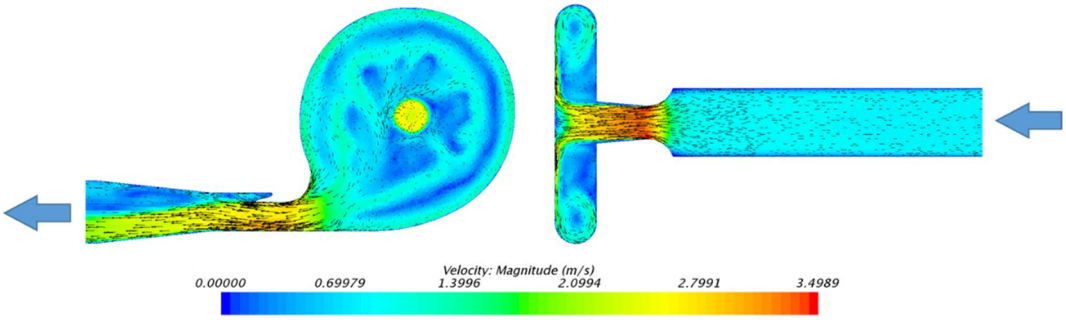

(a) Forward Flow mode

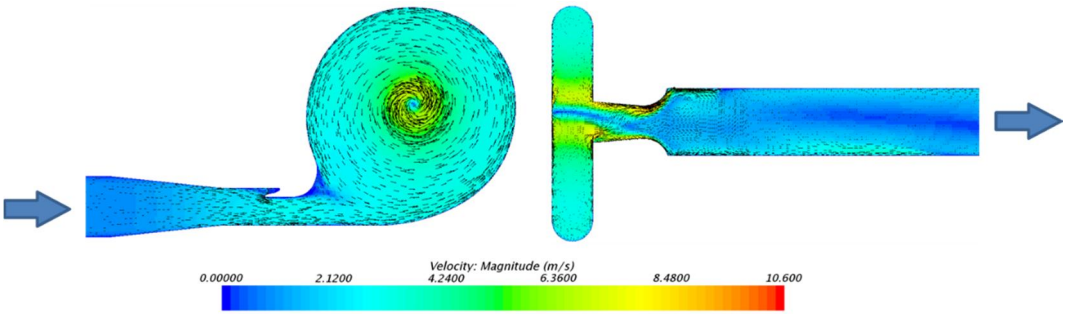

(b) Reverse flow mode

Figure 4.8 Flow configuration inside the topology optimized design

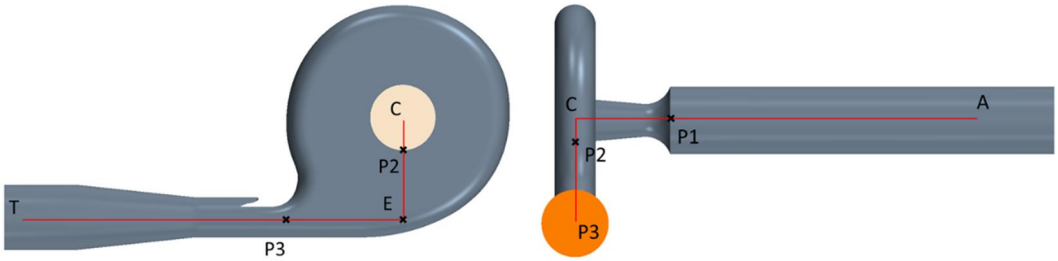

Figure 4.9 Schematic drawing for hypothetical lines and points

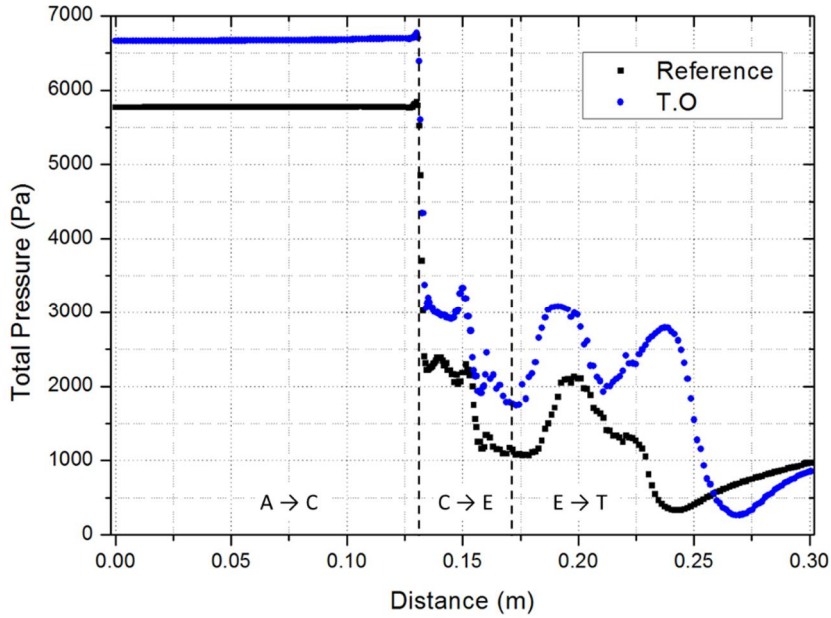

(a) Forward Flow mode

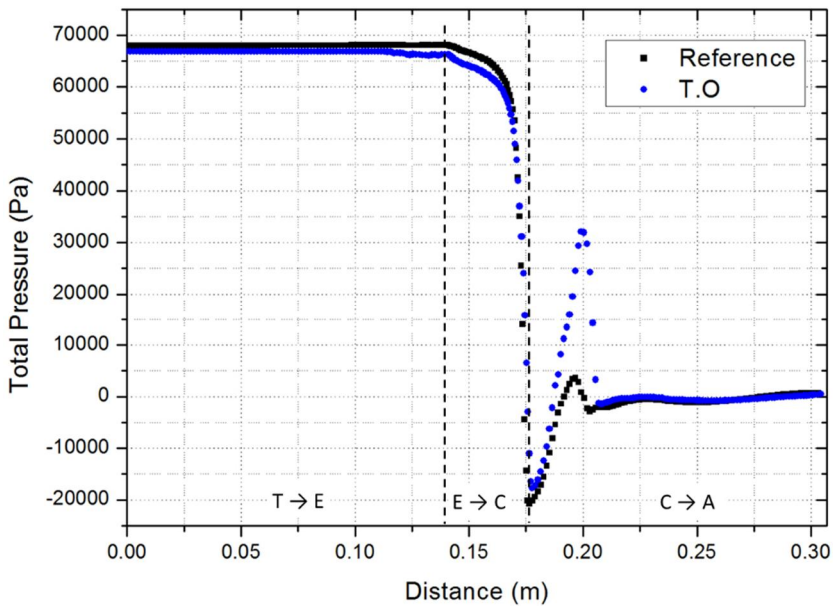

(b) Reverse flow mode

Figure 4.10 Total pressure distribution along hypothetical line

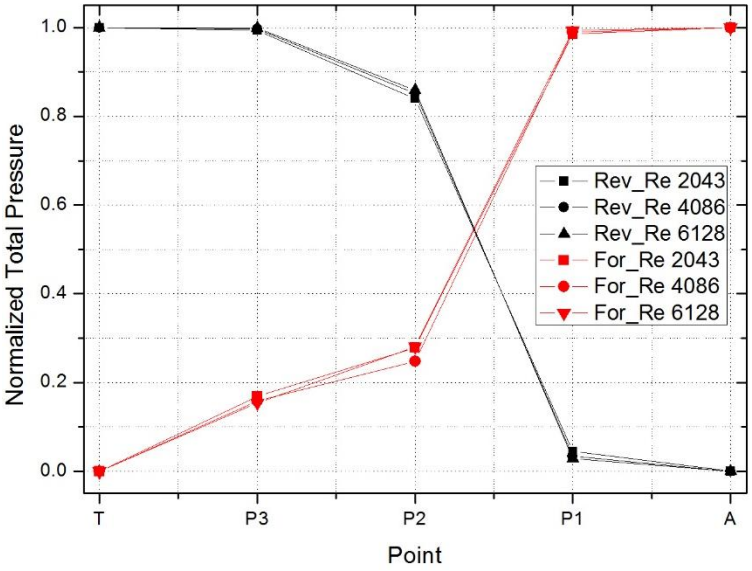

(a) Reference design

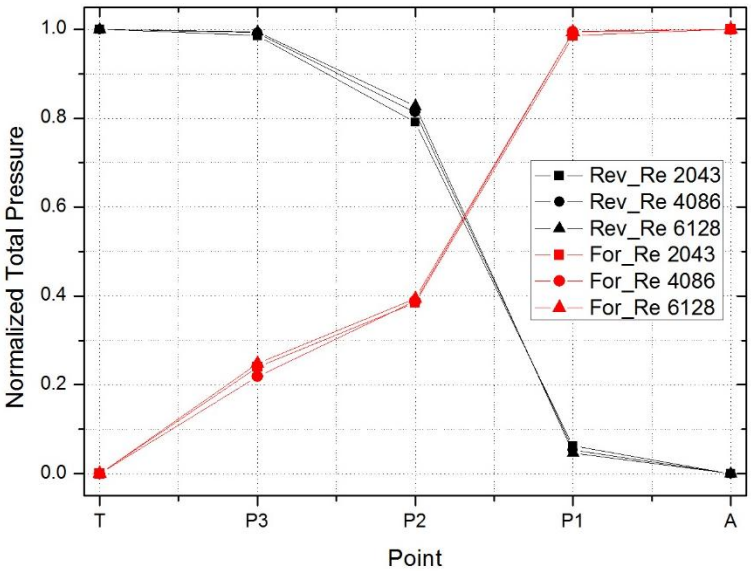

(b) T.O design

Figure 4.11 Normalized total pressure difference between hypothetical points

Chapter 5

Summary and Conclusions

5.1 Summary

In this study, vortex-type fluidic diode for advanced nuclear reactors was designed with topology optimization technique and the topology optimized design was studied through experimental and numerical analysis.

Topology optimization was conducted for tangential port and chamber with COMSOL multiphysics code. 2-D optimization geometry was selected as design domain and domain divided into two sub-domains to reduce design case. The optimization conducted in two steps in low Reynolds laminar flow regime. As a result, new topology optimized design with circular chamber, obstacle in tangential port and smooth connection between tangential port and chamber was acquired. Preliminary performance evaluation was conducted to validate topology optimized design in real boundary. Based on evaluated topology optimized design, 3-D part was designed.

To evaluate performance of 3-D topology optimized design, pressure drop measurement and flow visualization experiment were conducted. For comparison, test section for topology optimized design and reference design were made. The lab-scale test sections were produced using Stereolithography(SLA) 3-D printing

technique with epoxy resin. Pressure drop across the vortex-type fluidic diodes and velocity field of chamber in reverse flow mode were acquired in the inlet Reynolds number range from 2043 to 6128. Performance and velocity field for each design were compared.

Detailed 3-D CFD analysis was conducted to find out the reason for discrepancy between optimization results and experimental results. The specialized CFD software STAR-CCM+ was selected as analysis tool and grid generation tool. Analysis conducted for several flow condition with laminar flow model and turbulence model. Pressure drop across the vortex-type fluidic diodes and velocity field of chamber acquired as a result of CFD analysis were compared with experimental results. Total pressure change between specific point was measured and compared to confirm contribution of each sub-part on pressure drop. Then total pressure change in same sub-part for different design was compared to verify the effect of design modification in topology optimized design. From these studies, reason for discrepancy was identified.

5.2 Recommendations

Design acquired in this study has lower performance than reference design because optimization conducted for chamber periphery and tangential port. Therefore, the performance of the vortex-type fluidic diode is expected to be improved when the optimization conducted in new perspective. The optimization and parametric study for junction with axial port and chamber is strong candidate for optimization approach, considering contribution of this sub-part.

In this study, experimental condition was restricted because of cavitation

phenomenon. The experiment is required to be conducted in the high Reynolds number condition for wide range of application. For suppress cavitation, it is essential to modify the test loop to enable pressurization.

In addition, the CFD analysis conducted in only one grid condition. It is suggested to conduct grid sensitivity study to enhance the quality of CFD analysis.

Nomenclature

D	Tangential port diameter (m)
D_{AE}	Axial port diffuser diameter (m)
D_{AO}	Axial port expansion diameter (m)
D_{tO}	Tangential port diffuser diameter (m)
Di	Diodicity
Eu	Euler number
$\bar{f}_d$	Darcy friction force
h	Chamber height (m)
I	Turbulence intensity
L_A	Length of axial port (m)
L_{tan}	Length of tangential port (m)
$L_{tan,dif}$	Length of tangential port diffuser (m)
L_{ent}	Length of entrance region (m)
$L_{ent,a}$	Length of axial port entrance region (m)
$L_{div,a}$	Length of domain 2 in domain division a (m)
$L_{div,b}$	Length of domain 2 in domain division b (m)
l_T	Turbulence length scale
P	Pressure (Pa)
q	Convexity control parameter in Brinkman penalization
r	Distance from vortex center (m)
R	Chamber Radius (m)
R	Constraints of topology optimization
Re	Inlet Reynolds number

r_{AE}	Axial port connection radius (m)
s	Flow variable
$\bar{u}$	Flow velocity (m s^{-1})
V	Total volume of material (m^3)
v_t	Average velocity magnitude in tangential port (m/s)
w	Chamber width (m)
y^+	Dimensionless wall distance

Greek Letters

α	Degree of impermeability (kg s^{-1} m^{-3})
α_L	Lower limit of degree of impermeability (kg s^{-1} m^{-3})
α_U	Upper limit of degree of impermeability (kg s^{-1} m^{-3})
γ	Density function
ΔP	Pressure drop (Pa)
ε	Optimization convergence residual criteria
λ	Adjoint variable
μ	Viscosity (Pa s)
ρ	Density (kg m^{-3})
Φ	Objective function of topology optimization
Ω	Design domain of topology optimization
$d\Omega$	Design domain boundary of topology optimization

Subscripts

a	Design domain division a
b	Design domain division b
forward and *f*	Forward flow mode
reverse and *r*	Reverse flow mode

References

Borrvall, T., Peterson, J., “Topology optimization of fluids in Stokes flow”, *International Journal for Numerical Methods in Fluids*, vol. 41, pp. 77-107, 2003

Chikazawa, Y., Aizawa, K., Shiraishi, T., Sakata, H., “Experimental Demonstration of Flow Diodes Applicable to a Passive Decay Heat Removal System for Sodium-Cooled Reactors”, *Jounal of Nuclear Science and Technology*, vol. 46, pp. 321-330, 2009.

COMSOL, COMSOL Multiphysics CFD Module User’s Guide, Ver. 5.1, 2015.

Holcomb, D. E., Cetiner, S. M., Flanagan, G. F., Peretz, F. J., Yoder, Jr., G. L., “An Analysis of Testing Requirements for Fluoride Salt-Cooled High Temperature Reactor Components”, ORNL/TM-2009/297, Oak Ridge National Laboratory, 2009.

Kulkarni, A. A., Ranade, V. V., Rajeev, R., Koganti, S. B., “CFD Simulation of Flow in Vortex Diodes”, *AIChE Journal*, vol. 54, pp. 1139-1152, 2008.

Kulkarni, A. A., Ranade, V. V., Rajeev, R., & Koganti, S. B., “Pressure drop across vortex diodes: Experiments and design guidelines”, *Chemical Engineering Science*, vol. 64, pp. 1285-1292, 2009

Lin, S., Zhao, L., Guest, J. K., Weihs, T. P., Liu, Z., "Topology Optimization of Fixed-Geometry Fluid Diodes", *Journal of Mechanical Design*, vol. 137, 2015.

Lv, Q., Chen, M., Sun, X., Christensen, R., Blue, T., Yoder, G., ... & Sabharwall, P., "Design of fluidic diode for a high-temperature DRACS test facility", In *2013 21st International Conference on Nuclear Engineering*, pp. V004T09A123-V004T09A123. American Society of Mechanical Engineers, 2013

Othmer, C., de Villiers, E., & Weller, H., "Implementation of a continuous adjoint for topology optimization of ducted flow", In *18th AIAA Computational Fluid Dynamics Conference*, pp. 3947, 2007

Pandare, A., & Ranade, V. V., "Flow in vortex diodes", *Chemical Engineering Research and Design*, vol. 102, pp. 274-285, 2015.

Priestman, G. H. "A study of vortex throttles Part 1: Experimental", *Proceedings of the Institution of Mechanical Engineers, Part C: Journal of Mechanical Engineering Science*, vol. 201, pp. 331-336, 1987.

PIVTEC, PIV view 2C/3C User manual, version 3.6.3, 2015

Serin Shin, J. H. Jeong, D. K. Lim, E. S. Kim, "Topology Optimization on SFR Fluidic Diode Axial port and Computational Fluid Dynamics Analysis", *17th International Topical Meeting on Nuclear Reactor Thermal Hydraulics (NURETH-17), Xi'an, China*, 2017

Song, M. S., Choi, H. Y., Seong, J. H., & Kim, E. S., “Matching-index-of-refraction of transparent 3D printing models for flow visualization”, *Nuclear Engineering and Design*, vol. 284, pp. 185-191, 2015

SIEMENS PLM, STAR-CCM+ user manual, version 12.04, 2017

Yoon, G. H., “Topology optimization for turbulent flow with Spalart–Allmaras model”, *Computer Methods in Applied Mechanics and Engineering*, vol. 303, pp. 288-311, 2016

Zhang, H., Zhao, H., Davis, C., Memmott, M., “RELAP5 Analysis of the Hybrid Loop-Pool Design for Sodium Cooled Fast Reactors”, International Congress on Advances in Nuclear Power Plants (ICAPP 2008), Anaheim, California, USA, 2008.

Zhao, H., Zhang, H., Mousseau, V. A., Peterson, P. F., “Improving SFR Economics Through Innovations from Thermal Design and Analysis Aspects”, International Congress on Advances in Nuclear Power Plants (ICAPP 2008), Anaheim, California, USA, 2008.

Appendix A

Safety Analysis for Advanced Nuclear Reactors

This section summarizes the previous study safety analysis result for hybrid loop-pool type SFRs and DRACS facility of FHRs

In previous study, safety analysis was conducted with RELAP5 safety analysis code to verity the design concept of hybrid loop-pool type SFRs (Zhang et al., 2008). The safety analysis simulated the LOFC with reactor scram condition with Relap5 model as shown in Fig A.1. This model represents the components in hybrid loop-pool type SFRs including hot and cold pool, reactor core and IHX and PHX. The four PHX module are represented in component 630, and this component is connected to fluidic diode junction. Flow resistance of fluidic diode junction is 1 for downward flow and 400 for upward flow. More detailed parameter for RELAP5 model was listed in Table A.1. The initial condition for transient analysis was listed in Table A.2. From start of transient, primary pump coasts down about 200s. During coast down, natural circulation flow is developed to provide adequate coolant flow. Fig A.2 shows the mass flow rate through PHX in transient condition. It was found that mass flow through PHX in LOFC transient reaches up to 14kg/s, equivalent to Reynolds number 108824 at fluidic diode junction.

To evaluate the thermal performance of DRACS system of FHRs, safety analysis was conducted with self-developed MATLAB code in previous study (Lv,

Q, et al. 2015). Safety analysis was conducted for two scenarios. In first one, pump is tripped at start of simulation with constant core power of 10kW. In second one, pump works at start of simulation with flow rate of 5.422kg/s and core power is 9kW. After system reaches to steady state, pump is tripped and core power is changed to 10kW. Initial condition of both scenarios are same with 500℃ for primary and secondary coolant temperature and 40℃ for temperature in air loop. Fig A.3 and Fig A.4 shows the primary coolant mass flow rate. It was found that primary coolant mass flow rate reaches up to 0.12 kg/s, equivalent to Reynolds number 2381 at fluidic diode inlet.

Table A.5 Detailed parameters for RELAP5 model (Zhang et al., 2008)

Parameter	Values
Intermediate Heat Exchanger (IHX)	
Heat transfer capacity (MWth)	125
Number of tubes per heat exchanger	3300
Tube pitch-to-diameter ratio	1.40
Tube outer diameter (c)	1.59
Active tube length (m)	3.85
Central tube outer diameter (cm)	40.6
PRACS Heat Exchanger (PHX)	
PHX length (m)	2
PHX connecting pipe diameters (cm)	12.5
PHX pitch-to-diameter ratio	2
PHX tube outer diameter (cm)	2
Number of tubes per PHX	20
Hot Pool Volume (m^3)	77.2
Buffer Pool Volume (m^3)	146.8

Table A.6 Initial condition for the transient analysis (Zhang et al., 2008)

Parameter	Values
Primary Coolant System	
Core power (MW)	250
Mass flow rate (kg/s)	1242
Core inlet temperature (°C)	355
Core outlet temperature (°C)	510
Peak cladding temperature (°C)	540
Primary pump specific speed (RPM)	283
Mass flow rate through PHXs (kg/s)	14.5
Buffer Pool Temperature (°C)	355

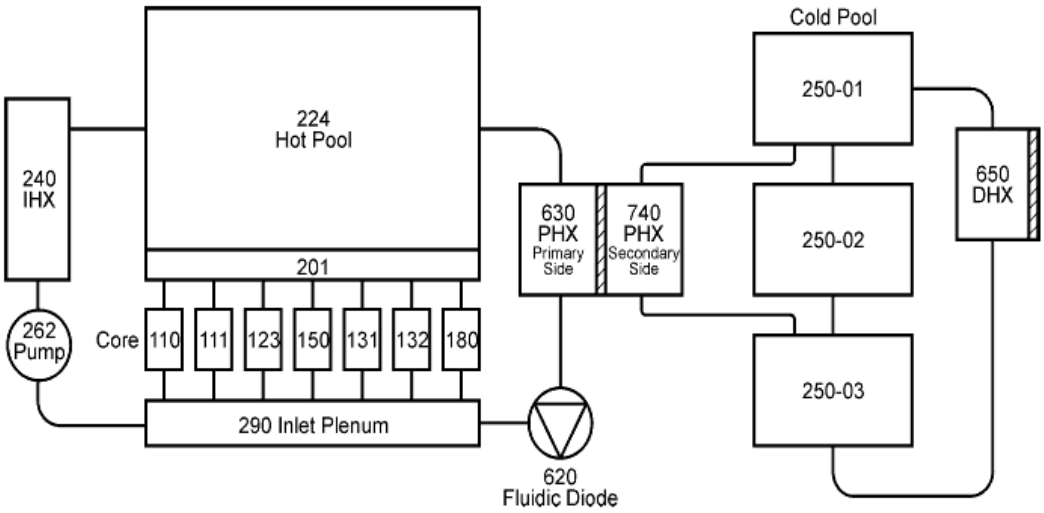

Figure A.1 RELAP5 model for hybrid loop-pool type SFRs (Zhang et al., 2008)

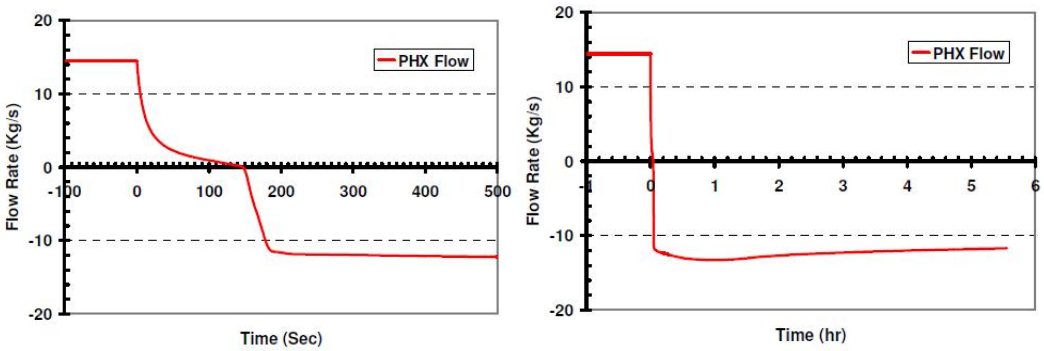

(a) For 500 second after LOFC (b) For full-time scale

Figure A.2 Mass flow rate flow through PHX during LOFC transient (Zhang et al., 2008)

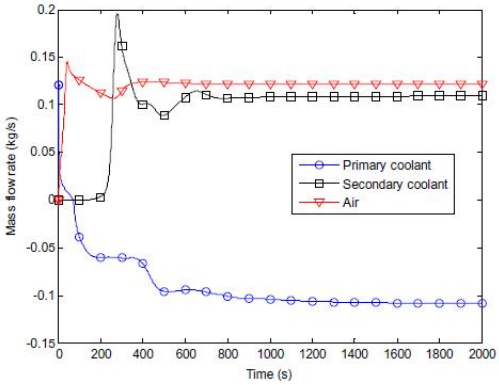

(a) For 2000 second after transient

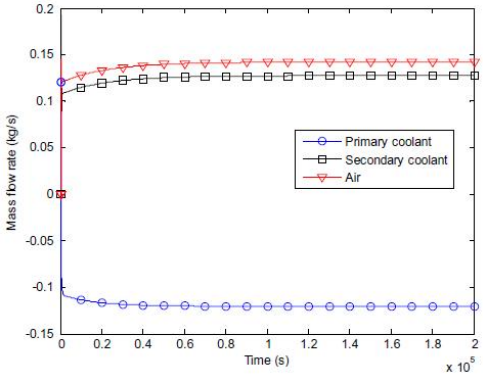

(b) For full-time scale

Figure A.3 Coolant Mass flow rates in first scenario (Lv, Q, et al. 2015)

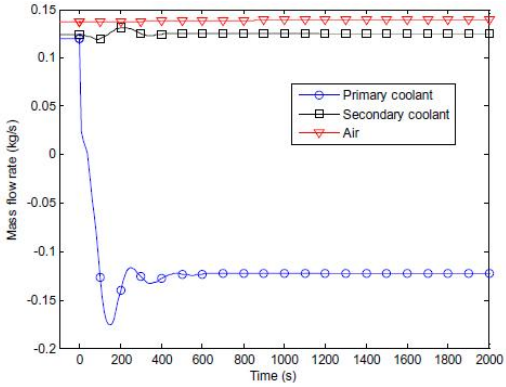

(a) For 2000 second after transient

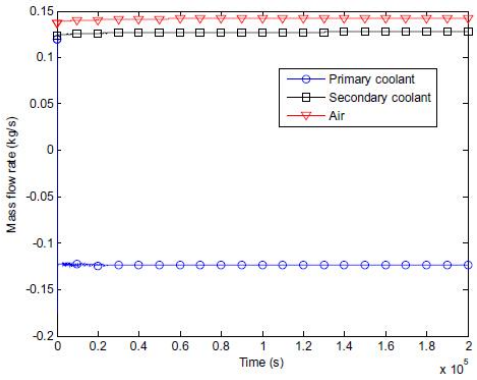

(b) For full-time scale

Figure A.4 Coolant Mass flow rates in second scenario (Lv, Q, et al. 2015)

국문 초록

Fluidic diode는 정방향 유동에 대해서는 작은 유동 저항을 인가하고, 역방향 유동에 대해서는 큰 유동 저항을 인가하는 단순한 피동형 유동 장치이다. 이 장치는 하이브리드 루프-풀 소듐냉각고속로와 용융염냉각로와 같은 차세대원전에 적용되어 자연대류를 통한 피동 냉각 개념을 구현하는데 있어 중요한 역할을 수행한다. Vortex-type Fluidic diode는 fluidic diode 개념 중 하나로, 원형 챔버와 두개의 원형 포트로 구성되어 있다. 해당 개념은 그 구조가 간단하고, 유지보수가 쉽다는 장점 때문에 원자력 분야에서 선호되고 있으며, 최근까지 그 성능을 향상시키기 위한 연구들이 진행되고 있다. 따라서 본 연구에서는 위상최적화 기법을 통하여 vortex-type fluidic diode의 새로운 설계를 제안하였다.

위상최적화는 특정 설계 영역의 최적의 물질 분포를 찾는 최적화 기법으로, 해당 기법을 활용해 기존에 제안되지 않은 새로운 설계를 얻을 수 있다. 본 연구에서 위상최적화는 접선 포트와 챔버의 설계에 적용되었으며, 그 과정은 2차원 영역에서 저유속 층류 유동 조건하에 수행되었다. 최적화 결과 중 가장 명확한 경계를 가지며 성능이 향상된 결과를 최적 설계로 선정하였다. 최적 설계의 성능 검증을 위해 2차원 층류 전산유체해석이 수행되었으며, 2차원 설계를 바탕으로 3차원 형상 설계를 수행하였다.

3차원 최적 설계의 성능을 검증하기 위하여, 최적 설계와 기존

설계에 대해서 압력 측정과 유동 가시화 실험이 이루어졌다. 실험 시편은 SLA 3D 프린팅 기법을 통해 제작되었으며, 유동가시화에는 MIR-PIV 기법이 활용되었다. 각 설계의 유동장과 압력강하가 비교되었으며, 그 결과 기존 설계가 더 나은 성능을 가지는 것을 확인하였다.

최적 설계의 설계 변경이 압력 강하에 미치는 영향을 확인하기 위해, 3차원 전산유체해석을 통한 유동 특성 연구가 수행되었다. 전산유체해석을 통해 실험 조건을 모사하였으며, 층류 모델과 난류 모델을 모두 적용하여 실험 결과를 보다 잘 예측하는 모델을 선정하였다. 유동장과 전압과 같은 유동 변수들에 대해서 연구를 수행하였으며, 그 결과 vortex-type fluidic diode의 부분 구조의 압력 강하에 대한 기여도를 평가 하였다.

주요어

위상최적화, 유동 다이오드, 전산유체해석, 유동 가시화

학번: 2016-21306